UNIVERSITÀ DEGLI STUDI DI PADOVA

DIPARTIMENTO DI FISICA E ASTRONOMIA "G. GALILEI"

Corso di Laurea in Astronomia

Tesi di Laurea Magistrale

CHARACTERIZATION OF THE MULTIPLE PLANETARY SYSTEM *Kepler*-279 USING TRANSIT TIME VARIATIONS

Relatore:
Prof. Giampaolo Piotto
Correlatori:
Dott. Luca Borsato
Dott. Valerio Nascimbeni

Laureanda: **Gaia Lacedelli**
Matricola: 1155365

Anno Accademico 2017/2018

A mia nonna Wilma,
per aver sempre vegliato su di me.

A mia nonna Mirella,
la donna più forte che io abbia mai conosciuto,
modello ed esempio.

CONTENTS

ABSTRACT

Exoplanets in multi-planet systems have non-Keplerian orbits due to gravitational interactions, that can cause transit time variation (TTV) and transit duration variation (TDV). The TTV technique is a powerful tool to detect and characterize extra-solar planets.

I used the TTV technique to characterize the planetary system *Kepler*-279 (K279), with a particular emphasis on the mass determination. K279 is an F-type star ($T_{\rm eff} = 6363$ K, $R_\star = 1.52\,R_\odot$, $M_\star = 1.10\,M_\odot$) hosting three confirmed transiting planets ($R_{\rm b} = 3.51 \pm 0.79\,R_\oplus$, $R_{\rm c} = 5.08 \pm 0.58\,R_\oplus$, $R_{\rm d} = 4.55 \pm 0.46\,R_\oplus$) and one candidate planet ($R_{\rm KOI} = 4.13^{+0.69}_{-0.92}\,R_\oplus$). K279c and K279d show a strong, anti-correlated TTV signal, probably due to the periods ($P_{\rm c} = 35.735$ d, $P_{\rm d} = 54.420$ d) commensurability, that suggests a 3:2 first-order mean motion resonance (MMR). I applied the BLS (Box-fitting Least Squares) analysis to the *Kepler* short cadence light curve, removing iteratively the signal of the transit corresponding to the main peak in the periodogram, and I found no signal corresponding to the candidate proposed in the *Kepler* pipeline, that I classified as a False Alarm.
I exploited the TTV signal running three sets of simulations of a 3-planets system with `TRADES` (TRAnsits and Dynamics of Exoplanetary Systems), a Python code that simulates an N-body system. During the orbital integration, `TRADES` calculates the transit times and compares them with the observations, modelling the dynamics, and architecture, of multi-planet systems.
K279b has no TTV sinusoidal modulations and it does not gravitationally perturb the other planets (and vice versa), so it is not possible to put strong constraints on its mass using this technique. Concerning the planets c and d, I found two different sets of solutions, with high and low orbital eccentricities respectively. I applied the Frequency Map Analysis to check for the stability of the system in the two cases, and I found that the only stable configuration (in a timespan $t = 10^5$ yr) is the high-eccentricity one. I adopted as final solution the corresponding set of orbital parameters, with $M_{\rm c} = 14.49^{+1.82}_{-5.55}\,M_\oplus$ and $M_{\rm d} = 8.07^{+1.81}_{-3.14}\,M_\oplus$. This configuration seems to exclude a migratory history and suggests the so-called *inside-out* formation scenario, that is the outer planet forms after the inner one, through the creation of a gravitationally unstable gas ring located in the resonant orbit (Chatterjee & Tan 2014).

The analysis demonstrates the crucial role of the TTV technique in the characterization of planetary systems, in particular to study the mass-radius

relation and to understand the dynamical processes of formation and evolution. Currently this topic is extremely important. In fact, the application of TTV is expected to give a large contribution to the bulk characterization (radius, mass and therefore density) of exoplanets discovered by the forthcoming TESS, CHEOPS and PLATO missions.

SOMMARIO

I pianeti extra-solari che si trovano in sistemi planetari multipli hanno orbite non Kepleriane dovute alle mutue interazioni gravitazioni, le quali possono causare variazioni dei tempi di transito (TTV) e variazioni della durata del transito (TDV). La tecnica dei TTV è un'importante strumento utilizzato per rivelare e caratterizzare i pianeti extra-solari.

Ho utilizzato la tecnica dei TTV per caratterizzare il sistema planetario multiplo *Kepler*-279 (K279), con particolare attenzione alla determinazione delle masse planetarie. K279 è una stella di sequenza principale di tipo spettrale F ($T_{\rm eff} = 6363$ K, $R_\star = 1.52\,R_\odot$, $M_\star = 1.10\,M_\odot$), che ospita tre pianeti transitanti confermati ($R_{\rm b} = 3.51 \pm 0.79\,R_\oplus$, $R_{\rm c} = 5.08 \pm 0.58\,R_\oplus$, $R_{\rm d} = 4.55 \pm 0.46\,R_\oplus$) ed un candidato pianeta ($R_{\rm KOI} = 4.13^{+0.69}_{-0.92}\,R_\oplus$). K279c e K279d mostrano un segnale TTV forte ed anti-correlato. probabilmente dovuto al rapporto tra i periodi ($P_{\rm c} = 35.735$ d, $P_{\rm d} = 54.420$ d), che suggerisce una risonanza di moto medio (MMR) 3:2. Ho applicato l'analisi BLS (Box-fitting Least Squares) alla curva di luce, sottraendo iterativamente il segnale del transito corrispondente al picco principale del periodogramma. Non avendo trovato un segnale corrispondente al candidato proposto dalla pipeline di *Kepler*, ho classificato il candidato come un *False Alarm*.

Ho utilizzato il segnale TTV per effettuare tre set di simulazioni con `TRADES` (TRAnsits and Dynamics of Exoplanetary Systems), un codice Python che simula sistemi ad N-corpi. Durante l'integrazione numerica, `TRADES` calcola i tempi di transito e li confronta con quelli osservati, modellando la dinamica e l'architettura di sistemi planetari multipli.

K279b non mostra una andamento TTV sinusoidale e non sembra perturbare gravitazionalmente gli altri pianeti (e viceversa). Pertanto, non è stato possibile ottenere dei vincoli sulla sua massa utilizzando questa tecnica. Per quanto riguarda i pianeti c e d, ho ottenuto due diversi set di soluzioni, uno ad alta ed uno a bassa eccentricità. Ho utilizzato la *Frequency Map Analysis* per testare la stabilità del sistema in entrambi i casi: l'unica configurazione stabile in un tempo-scala di 10^5 anni è risultata essere quella ad alta eccentricità. Conseguentemente, ho scelto come soluzione finale il corrispondente set di parametri, ottenendo come valori di massa $M_{\rm c} = 14.49^{+1.82}_{-5.55}\,M_\oplus$ e $M_{\rm d} = 8.07^{+1.81}_{-3.14}\,M_\oplus$. Una tale configurazione sembra escludere la possibilità di formazione del sistema tramite migrazione, suggerendo invece il cosiddetto scenario di formazione *inside-out*. Secondo tale scenario, il pianeta interno, più massivo, si forma per primo ed induce la formazione

del pianeta più esterno creando, tramite instabilità gravitazionale, un anello di gas nell'orbita risonante (Chatterjee & Tan 2014).

L'analisi effettuata dimostra il ruolo cruciale della tecnica dei TTV nella caratterizzazione dei sistemi planetari, in particolare per lo studio del diagramma massa-raggio e per comprendere i processi di formazione ed evoluzione. Attualmente, tale campo di ricerca è di estrema importanza: infatti, la tecnica dei TTV contribuirà in modo significativo alla caratterizzazione (massa, raggio e conseguentemente densità) degli esopianeti che verranno individuati dalle future missioni TESS, CHEOPS e PLATO.

INTRODUCTION

Since the discovery of the first planet orbiting a star different from the Sun (51 Peg-b, Mayor & Queloz 1995), the exoplanetary science grew enormously in the last two decades, leading to a new, prolific field that involves different disciplines of astrophysics and planetary science.

We have now the possibility to study a considerable number of exoplanets and exoplanetary systems, thanks to the development and improving of different discovery techniques, that allowed us to highlight the incredible complexity and variety of the planetary configurations hosted by the neighbour stars. In particular, the transit technique is considered the most fruitful discovery method: over a total number of 3774 known exoplanets[1], more than 2600 have been discovered in this way thanks to the spacecraft *Kepler* (including also the *K2* mission) and ground-based surveys, e.g. HAT-Net and WASP. All these bodies have a radius measurement, since the planetary radius is one of the parameters that can be determined using the transit technique. However, this method does not provide any information about the mass of the transiting planet. The planetary mass is the second essential quantity needed for a first bulk characterization of a planet: indeed, once radius and mass are know, the average density can be determined, allowing the discrimination between gaseous and rocky planets and so providing a first clue about the habitability. Radius, mass and density are also important properties used to investigate the processes of formation and evolution, since they can provide constraints on the theoretical models based on the study of the Equation of State (EoS). These quantities also allow us to improve the knowledge of the mass-radius relation, architecture, dynamics, and stability of exoplanetary systems.

The most common method used for the mass determination is the Radial Velocity (RV) technique, based on the gravitational interaction between the star and the planet. In fact, the two bodies orbit around the common center of mass and this motion induces, along the radial direction, a Doppler effect than can be measured in the stellar spectrum thanks to the spectral lines shift. However, in the last years a second method for the mass determination has become more and more important and solid: it is the Transit Time Variations (TTVs) technique (Miralda-Escudé, 2002; Agol et al., 2005). In principle, a single planet on a Keplerian orbit should be seen to transit at regular time intervals. However, if there were a second planet (not necessarily transiting)

[1] From the NASA Exoplanet Archive in date 02/08/2018, https://exoplanetarchive.ipac.caltech.edu/.

in the same system, it gravitationally perturbs the orbit of the transiting one: as a consequence, a variation in the measured mid-transit time relative to the unperturbed one is expected (Holman & Murray, 2005). After some spurious announcements of discovery of perturbing planets causing TTVs, the first convincing detection occurred with the *Kepler*-9 system, showing large-amplitude TTVs of two Saturn-sized planets (Holman et al., 2010). The *Kepler*-9 paper kicked off a series of discoveries of TTVs with the *Kepler* spacecraft, with now more that 200 systems showing TTVs (Holczer et al., 2016). The present state-of-the-art demonstrates that the TTVs technique is an excellent method for the discovery and characterization (in particular mass determination) of multiple planetary systems, with spectacular results, e.g. *Kepler*-11 (Lissauer et al., 2011), WASP-47 (Becker et al., 2015), and TRAPPIST-1 (Gillon et al., 2017). In fact, in many cases RV measurements cannot be obtained, either because the star is too faint or the RV amplitude K is too small to be detected by the current instruments. In this case, the only way to obtain planetary masses is the TTVs technique.

The purpose of this thesis is the characterization of the multiple planetary system *Kepler*-279, with a particular focus on the determination of orbital parameters and masses. In order to do that, I exploited the TTV signal measured from the light curve of the host star. The thesis is structured in the following way:

- **Chapter 1**: I first introduce in details the TTV technique, explaining the underlying dynamical principles and describing the TTV signal properties, and highlighting the advantages in the contest of the exoplanetary discovery techniques (Sec. 1.1). In Section 1.2 I describe the TRADES (TRAnsits and Dynamics of Exoplanetary Systems) code (Borsato et al., 2014), an N-Body integrator used to compute the orbits and to fit the TTV signals in order to determine the planetary orbital parameters and masses.

- **Chapter 2**: in this chapter I explain the steps for the target selection, I describe the chosen system, *Kepler*-279, and I present the detailed analysis performed to define the configuration and the physical parameters of the system.
  In Section 2.1 I illustrate the input catalog (Holczer et al., 2016), containing all the *Kepler* candidates showing TTV signals, and I explain my target selection criteria. In Sec. 2.2 I describe the selected system as reported in the catalog. I present the light curve analysis (Sec. 2.2.1) and the Box-fitting Least Squares method (Sec. 2.2.2), used to confirm or exclude the presence of a planetary candidate. Finally, I explain how I dealt with the different stellar parameters reported in literature (Sec. 2.2.3) and I summarize the adopted properties of the system.

- **Chapter 3**: this chapter contains the details of the dynamical analysis performed with TRADES. Section 3.1 describes the input parameters of all the simulations.
  I performed three sets of simulation. First, I fitted all the planetary masses (Simulation Set 1 – Sec. 3.2), then I fixed the one for which TTVs were uninformative (Simulation Set 2 – Sec. 3.3). Finally, I varied the inclination of the system, after calculating its value through a transit fit (Simulation Set 3 – Sec. 3.4). I considered different families of solutions according to their high or low eccentricity (Sec. 3.4.1, 3.4.2).

- **Chapter 4**: this chapter illustrates the stability analysis performed on the system. I describe the Frequency Map Analysis, a technique that exploits the numerical orbital integration (performed with the `SyMBA` code) to determine the system stability through the study of the dominant frequencies (Sec. 4.1). In the following sections I discuss the stability analysis of a representative sample of both high and low eccentricity solutions, in order to identify the final, unique solution.

  Finally, I present a summary of the results and I discuss them, considering the present state-of-the-art. I describe the possible outlooks of this work, taking into consideration also the present and future missions related to exoplanets, mainly TESS and CHEOPS, but also PLATO.

1 TRANSIT TIME VARIATIONS TECHNIQUE

In the Kepler (two-body) problem, the gravitational potential gives rise to closed orbits, and in absence of perturbations the trajectory is strictly periodic with period $P = 2\pi a^{3/2}(GM)^{-1/2}$. According to this law, using Tycho Brache's data for planetary positions, Kepler showed that the planets of the Solar System were moving on elliptical orbits around the Sun, located in one focus. However, during the XVII century, it has been noticed that the orbits of Jupiter and Saturn did not really obey the Keplerian model. Considering their little anomalies, Laplace developed a perturbation theory and used the mass derived from their satellites orbits to explain the deviations of the trajectories. Later, Urban Le Verrier exploited the changes in Uranus orbit to predict the position of an unknown, perturbing planet. Neptune was subsequently observed within a degree of the predicted position (Kollerstrom, 2001). The interactions among three or more bodies due to the gravitational force are the base of the Transit Time Variations (TTVs) technique: indeed, transiting exoplanets in multiple planetary systems have non-Keplerian orbits that cause the times and the duration of the transit to vary. Like most of the tools for discovering and characterizing exoplanets, the TTV technique is an indirect method, that is to say it allows us to infer planetary parameters by analyzing the effects on the host star.

If more than one planet is present in a system, an additional force to that of the gravity of the star has to be considered, and the total force acting on planet 1 is:

$$\boldsymbol{F_1} = -G\mu_1 M r_1^{-2}\hat{\boldsymbol{r}}_\mathbf{1} + \boldsymbol{F_{12}}\,, \tag{1}$$

where G is the universal gravitational constant, μ_1 is the reduced mass, M is the total mass, and $\boldsymbol{r_1} = (x, y, z)$ is the vector stretching from the star to the planet. The first term is gravitational force exerted by the star and $\boldsymbol{F_{12}}$ is the additional force exerted by the second planet with mass m_2. This last term has the expression:

$$\boldsymbol{F_{12}} = \mu_1 \ddot{\boldsymbol{r}}_\mathbf{1} = G\mu_1 m_2 |r_2 - r_1|^{-3}(\boldsymbol{r_2} - \boldsymbol{r_1}) - G\mu_1 m_2 r_2^{-2}\hat{\boldsymbol{r}}_\mathbf{2}\,. \tag{2}$$

The first term is the direct gravitational acceleration of planet 1 due to planet 2, while the second term is an indirect frame-acceleration effect, due to the acceleration of the star caused by the second planet.

A Keplerian orbit has a strictly constant period P and the transit central time (or mid-transit time) can be described with a linear ephemeris

$$T_{\rm lin} = T_{\rm ref} + P \times E\,, \tag{3}$$

where E is the epoch – an integer transit number – and $T_{\rm ref}$ is the time of the transit with $E = 0$. Gravitational perturbations cause timing deviation from a Keplerian model: the variations of the mid-transit time induced by the perturbations are the so-called Transit Time Variations (TTVs), a term coined by Agol et al. (2005). The TTV signal is represented in the $O - C$ diagram (O minus C; Sterken 2005), where O are the observed transit times and C are the linear transit times (Eq. 3). The model of the timing of WASP-47 is shown as an explanatory example in Fig. 1 (Becker et al., 2015).

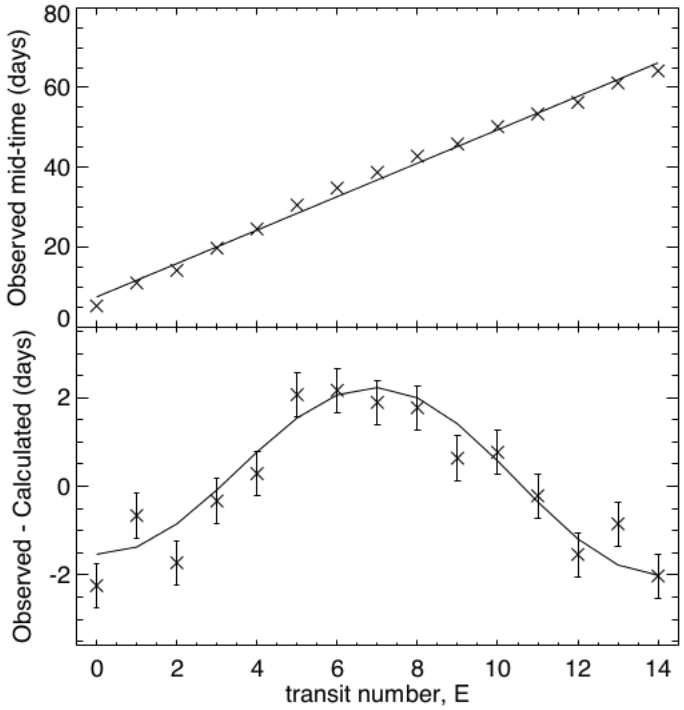

Figure 1: Explanatory model of the Transit Time Variations of WASP-47, with a greatly exaggerated perturbation. *Top panel*: measured transit central time, with a superimposed least-squares linear fit. *Bottom panel*: $O - C$ diagram, corresponding to the residual of the previous fit. A sinusoidal fit is plotted as a line. From Becker et al. (2015).

1.1 TTV SIGNAL PROPERTIES

To better understand the effect caused by a companion on a planetary orbit, and consequently the properties of the TTV signal, let us first summarize

the orbital elements, that are the parameters required to uniquely identify a specific orbit (Fig 2).

- Semi-major axis (a): it is half of the major axis (the line that runs through the center and both foci) of the elliptic orbit. It can be substituted by the period (P), using the Kepler's third law

$$P^2 = \frac{4\pi^2}{G(M_\star + M_\mathrm{p})}\, a^3 \,, \tag{4}$$

  where G is the universal gravitational constant and M_p, $M_\star$ are respectively the planetary and stellar masses.

- Eccentricity (e): it determines the amount by which an orbit deviates from a perfect circle, and it can be expressed in terms of the semi-major axis a and semi-minor axis b as

$$e = \sqrt{1 - \frac{b^2}{a^2}} \,. \tag{5}$$

  A value of 0 defines a circular orbit, while values between 0 and 1 define an elliptic orbit.

- Inclination (i): it is the angle between the orbital plane and the reference plane. In the case of exoplanets, the reference plane is the plane tangent to the celestial sphere at the point of interest (called the plane of the sky). An inclination of 0° (or 180°) defines a face-on orbit, meaning that the plane of the orbit is parallel to the sky. An inclination of 90° defines an edge-on orbit, with the plane of the orbit perpendicular to the plane tangent to the sky.

- Longitude of the ascending node (Ω): it is the angle from the reference direction to the direction of the ascending node (where the measured object moves away from the observer through the reference plane), measured counterclockwise in the reference plane.

- Argument of the pericenter (ω): it defines the orientation of the ellipse in the orbital plane and it is the angle measured in the direction of motion from the ascending node to the pericenter.

- True anomaly (ν) at time t_0: it is the angle between the direction of the pericenter and the position of the body at a specific time. It can be substituted by the mean anomaly ($\mathcal{M}$), that is the angular distance from the pericenter which a fictitious body would have if it moved in a circular orbit, with constant speed, in the same orbital period as the actual body in its elliptical orbit.[1]

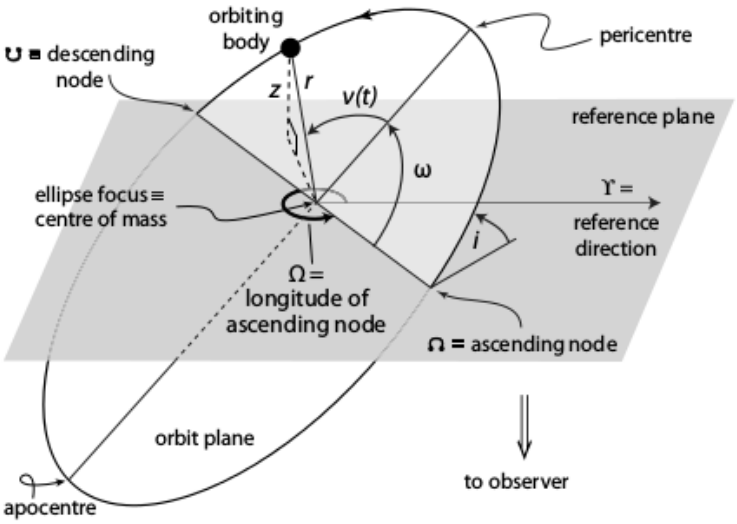

Figure 2: Orbital elements of a celestial body. In the case of extrasolar objects, the reference plane (gray) is tangent to the celestial sphere. From Perryman (2014).

Agol & Fabrycky (2017) have analyzed the TTV effect in the case of a 2-planet system and developed the following formulae, that allow us to compute the timing variations:

$$\begin{aligned}(O-C)_1 &= P_1 \frac{m_2}{m_0} f_{12}(\alpha_{12}, \theta_{12}) \,, \\ (O-C)_2 &= P_2 \frac{m_1}{m_0} f_{21}(\alpha_{12}, \theta_{21}) \,,\end{aligned} \tag{6}$$

where m_0, m_1, m_2 are respectively the masses of the star and of the two planets, P_1, P_2 are the two planetary periods, and f_{jk} is a function describing the perturbations caused by planet j on planet k, depending on the semi-major axis ratio, $\alpha_{jk} = \min(a_j/a_k, a_k/a_j)$, and on the angular orbital elements of the planets, $\theta_{jk} = (\mathcal{M}_j, e_j, \omega_j, i_j, \Omega_j, \mathcal{M}_k, e_k, \omega_k, i_k, \Omega_k)$. These functions are evaluated in a series of papers concerning the perturbation theory – Nesvorný & Morbidelli (2008), Nesvorný & Beaugé (2010), and Deck & Agol (2016) among them. The main consequences of equation 6 can be summarized as follows:

- The TTV signal $(O-C)$ of each planet depends only on the masses of the other bodies in the system. In fact, according to the Newton's second law and to the gravity's law, the acceleration of a body does not depend on its own mass.

[1] Note that $\mathcal{M}$ is a mathematically convenient angle which varies linearly with time, but which does not correspond to a real geometric angle.

- The amplitude of the TTV signal is proportional to the orbital period of each planet, since the gravitational interactions occur on the orbital timescales.

In the general case of N planets, under the assumptions that $m_j/m_0 \ll 1$ and none of the pairs of the planets are in, or close to, a mean-motion resonance (MMR)[2], the TTV signal of the j-th planet can be expressed as the linear combination of the perturbations due to each planet:

$$(O-C)_j = P_j \sum_{\substack{k=1 \\ k\neq j}}^{N} \frac{m_k}{m_0} f_{jk}(\alpha_{jk}, \theta_{jk})\,. \tag{7}$$

In systems out of resonance, also secondary TTV effects can be detected: for example, the presence of a body orbiting at very large distance can cause a TTV signal on an inner planet. The tide exerted by the external body causes the inner orbital period to slightly differ from the unperturbed one. A longer period is expected if the two bodies are coplanar, while a mutual inclination causes a shortening of the inner period. Moreover, since the tidal force scales with the third power of the distance, an eccentric outer orbit causes, in the inner orbit, period variations that have precisely the period of the outer orbit (Agol & Fabrycky, 2017). An other secondary effect that can contribute to the TTV signal is the torque of the inner orbit eccentricity caused by the presence of the outer companion (Borkovits et al., 2002).

1.1.1 Resonant systems

The description of the TTV signal properties of resonant systems is taken from (Agol & Fabrycky, 2017).
The presence of MMRs in multiple planetary systems is very interesting for the TTV technique. In these configurations the amplitude of the TTV signal is amplified, allowing also to characterize planets with small masses. The main contribution to the TTV signal is due to the orbital period change, which in turn is related to librations (including both librations in a, e and ψ – where ψ is the resonant angle – and the apocentric libration). A change $\delta P_1 \ll P_1$ in the orbital period of planet 1 leads to a change in the orbital period of planet 2:

$$\delta P_2 = -\delta P_1 \frac{m_1}{m_2} \left(\frac{P_1}{P_2}\right)^{5/3}. \tag{8}$$

[2] A mean motion resonance occurs when planetary orbits are dynamically coupled. The presence of a resonance is pointed out if the orbital periods are related by commensurabilities of the form $P_1/P_2 \simeq j/k$, where subscripts 1, 2 refer to the inner and outer planets, and j and k are small integers. The order of the resonance is $|j-k|$ (Perryman, 2014, Sec. 2.6).

Considering the Kepler's third law

$$a_2/a_1 = (P_2/P_1)^{2/3}\,, \tag{9}$$

and the energy equation

$$E = \frac{-Gm_0m}{2a}\,, \tag{10}$$

a change in P implies a change in a and consequently a change in E. Differentiating equations 9 and 10, and assuming the total energy conservation, we obtain Equation 8.
These changes lead to TTV cycles, whose period $P_{\rm TTV}$ (named "super-period" by Lithwick et al. 2012) depends only on the separation from the closest resonance, and it has the expression

$$P_{\rm TTV} = \frac{1}{|j/P_2 - k/P_1|}\,. \tag{11}$$

In the case of two transiting planets the characterization of a near-resonant system is extremely simplified, because the relative transit phase can be compared with the TTV phase. Lithwick et al. (2012) showed that, in the case of a near-first order MMR, the phase of the signal is predictable and the mutual gravitational interactions cause an anti-correlated sinusoidal signal. This expected $O-C$ shape can also be understood considering Equation 8. Over a fixed time interval, the inner planet has a factor P_2/P_1 more orbital period than the outer planet, and so the accumulated $O-C$ signal increases more than the one of the outer planet (by one factor of the period ratio) leading to

$$(O-C)_2 = -(O-C)_1 \frac{m_1}{m_2}\left(\frac{P_1}{P_2}\right)^{2/3}\,. \tag{12}$$

According to equation 12 we obtain anti-correlated TTV curves, which relative amplitudes are determined by the mass and period ratios. In the case of equal masses, the outer planet is expected to show a larger TTV amplitude, since the outer orbital size has to change more than the inner one, according to the orbital energy conservation. An example of observed anti-correlated TTV curves is shown in Fig. 3.

The amplitude of the TTV signal depends on both the mass of the perturbing planet and the eccentricity vectors of both planets (Lithwick et al., 2012). This leads to the so-called mass-eccentricity degeneracy, and in this case only an approximate mass scale can be determined. The degeneracy may be broken using an additional, independent periodic component of the TTVs, with a timescale other than the $P_{\rm TTV}$. Other components of TTVs have amplitudes that depend on the orbital parameters and masses in different ways, so the measurement of secondary components leads to additional, independent constraints on orbital parameters (Deck & Agol, 2015).

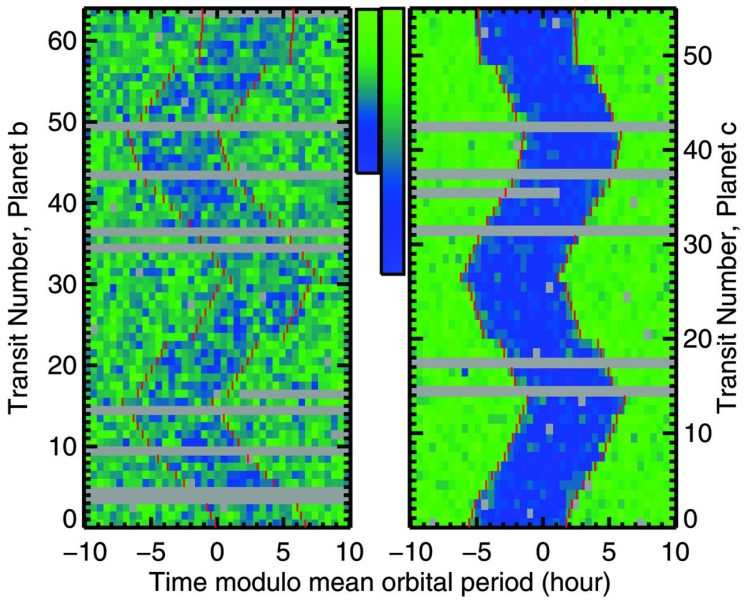

Figure 3: Anti-correlated TTV signal of the *Kepler*-36 system: *Kepler*-36b "river plot" is shown on the left, *Kepler*-36c is on the right. The relative flux scales with color (increasing from blue to green), with gray pixels representing unavailable data. Each row represents an individual light curve: the curved bands (conceiving the appellative "river plot") indicate a TTV perturbation, while strictly periodic transits would produce a vertical band. From (Holman et al., 2010).

In particular, the so-called short-timescale "chopping" TTV associated with the planetary synodic timescale[3] has been identified as an important feature for unique characterization of exoplanetary systems (Holman et al., 2010; Nesvorný et al., 2013). The chopping component induces a signal that alternates early and late on the top of the TTV sinusoidal with period $P_{\rm TTV}$, and it can be used to break the mass-eccentricity degeneracy (Deck & Agol, 2015). Let us consider two systems with the same period ratio, and same $P_{\rm TTV}$. Let us assume that the first system has zero eccentricity for both planets and an high value of the mass ratio, while the second has non-zero eccentricity for both planets and a small value of the mass ratio. The amplitude of the TTV signal due to the resonant term is the same for the two systems, but the chopping effect is stronger for the system with the larger mass ratio (Fig. 4). This effect has been detected in several cases and it has been used to uniquely determine the masses of some exoplanets (Schmitt et al., 2014; Deck & Agol, 2015).

[3] Non-resonant perturbations occur on the time between two consecutive conjunctions of the planets, that is when their separation is smaller and consequently the gravitational interaction is maximized. The period of the conjunctions is called synodic period and it has the expression $P_{\rm syn} = (1/P_1 - 1/P_2)^{-1}$ (Agol & Fabrycky, 2017).

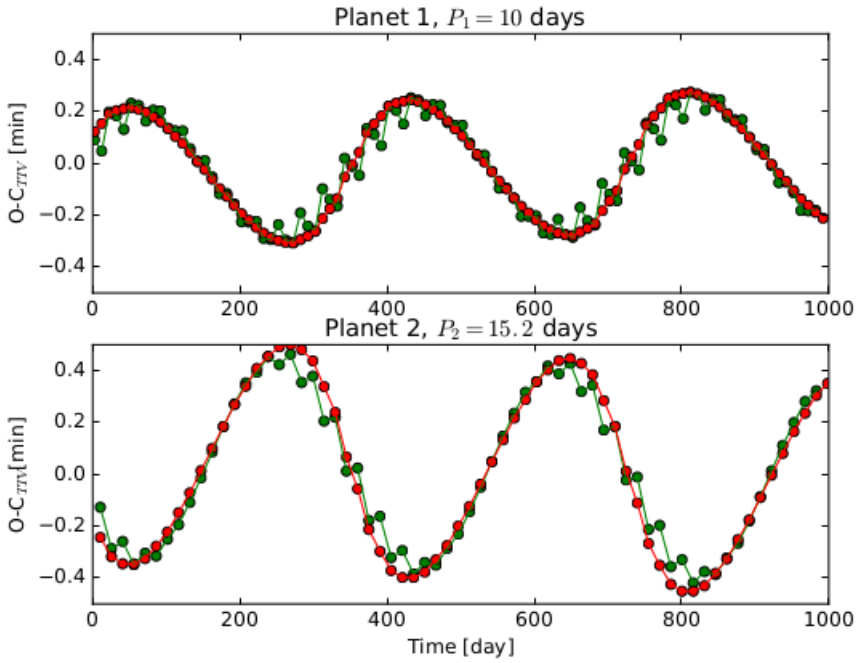

Figure 4: Comparison between the simulated TTVs of two low-eccentricity planets with larger mass ratios (green) and two high-eccentricity planets with smaller mass ratio (red). The chopping component is evident in the high-mass/low-eccentricity case, and less apparent in the low-mass/high-eccentricity case. From (Agol & Fabrycky, 2017).

Let us finally consider the case of only one transiting planet in a near resonant system. The TTV signal has a sinusoidal shape which could be produced by many different resonances of the perturbing planet. In this case, the set of degeneracies is exceptionally difficult to break and the characterization of non-transiting planets is an extreme task. Hence, in many cases it is possible to infer the presence of a companion through the detection of a TTV signal, but no information about its nature is available (with a few exceptions, such as *Kepler*-46 – Nesvorný et al. 2012).

1.1.2 RVs and TTVs

Transiting planets showing TTVs allow us to determine the planetary densities. In fact, the planetary-to-stellar radius ratio $R_p/R_\star$ can be inferred by the transit depth, while the TTV signal gives an estimate of $M_p/M_\star$, the mass ratio of the perturbing planet to the star. R_p and M_p can be derived if the stellar mass and radius are know, i.e. from photometry (Gray, 1967), asteroseismology (Ulrich, 1986), spectroscopy (spectroscopic gravity indicators for the mass), orbital dynamics for binary stars, or comparison with theoretical evolutionary models (Perryman, 2014). It is worth to note that

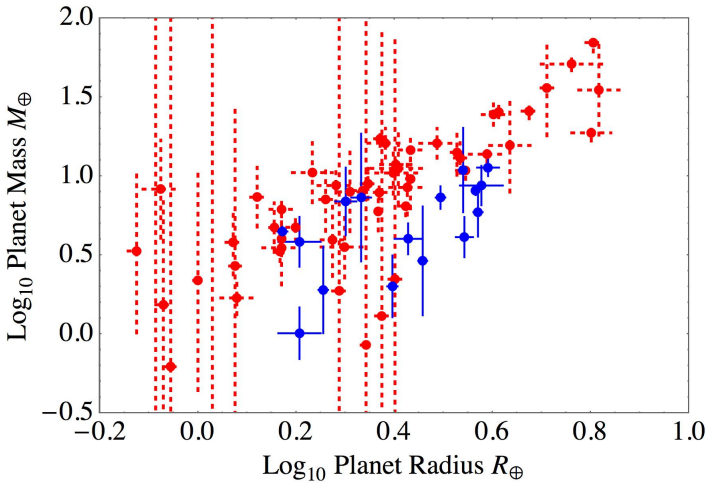

Figure 5: Observed mass and radius data as reported in Wolfgang et al. (2016), with TTV measured planets (blue) and RV measured planets (red). Note that the TTV masses are systematically lower than the RV masses. From Steffen (2016).

the knowledge of the planetary density is limited by how well the properties of the host star can be determined.

An alternative method to discover and characterize exoplanets is the Radial Velocity (RV) technique. The Doppler shift of the stellar lines due to the motion of the star around the barycenter of the star-planet system allows us to determine the quantity $M_p \sin i$, where i is the inclination. In the particular case of transiting planets, the inclination can be determined from the transit and consequently the planetary mass is known. Strong constraints on the properties of planetary systems can be deduced combining RVs and TTVs. However, in the rare cases of multiple systems with planetary masses determined using both methods, a discrepancy came out: as Figure 5 shows, TTV-discovered planets have smaller densities respect to the RV ones, at fixed radius[4] (Wolfgang et al., 2016). This discrepancy has been investigated by Steffen (2016), and the author connected it to observational biases. Steffen (2016), through the study of Markov Chain Monte Carlo simulations, has determined that the sensitivity of the two techniques to planetary mass varies with the properties of the planets themselves, leading to a bias in the observations. RV method is more sensitive to high mass planets, while the sensitivity of TTV is more uniform: at fixed radius, TTV can detect planets in a wider mass range with respect to RV (Fig. 6), especially at small radii ($R_p < 2\,R_\oplus$). This disparity can be explained by the different dependence

[4] The existence of extremely light planets – "puffy Neptunes" – has been pointed out using TTVs, and the most clamorous examples are *Kepler*-11e (Lissauer et al., 2011) and the *Kepler*-51 system (Masuda, 2014).

on the planetary parameters of the signal-to-noise ratio (SRN) of the two methods:

$$\mathrm{SNR_{RV}} \sim \frac{M_\mathrm{p}}{\sigma_\mathrm{RV}\, P^{1/3}}\,, \quad \mathrm{SNR_{TTV}} \sim \frac{M_\mathrm{p}\, R_\mathrm{p}^{2/3}\, P^{5/6}}{\sigma_\mathrm{TTV}}\,. \tag{13}$$

Therefore, TTV is more sensitive to planets with longer period and larger radius, while, for a given mass, RV planets will have systematically shorter orbits at the same SNR level. Planets orbiting close to their star may have thinner atmospheres, due to the strong stellar irradiation, and consequently higher densities: since the RV signal is stronger at shorter orbital periods, it would favor detecting planets with higher densities.

In addition to the dependence of the SNR of the two methods, other physical effects may induce changes in otherwise identical planets. One of those is a eventual relationship between a planet's properties and the likelihood that it resides in, or near, a MMRs (Steffen, 2016). In fact, planets near first-order MMRs may have a history of strong dynamical interactions – including possible couplings to the atmosphere (spin-orbit), that could significantly have affected the size of the planets. If the planets near MMRs are systematically larger, such a scenario may yield to the discrepancy observed in the density distribution, because a larger planetary radius reduces the timing uncertainty, and the TTV signal would be easier to detect (Steffen, 2016).

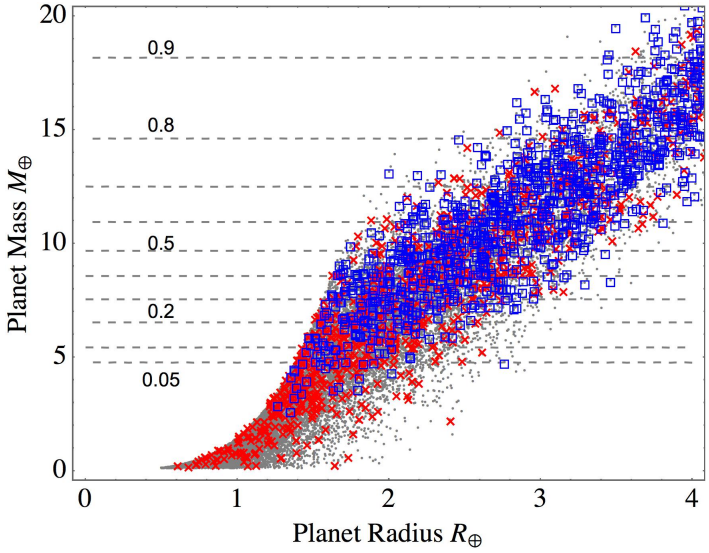

Figure 6: Mass and radius for all the simulated planets (gray dots) and an arbitrary subsample of detected planets using TTV (red crosses) and RV (blue squares), chosen for readability. Note that, especially for small radii, the RVs sample is biased toward more massive planets, while TTVs can be sensitive to less massive planets of the same size. From Steffen (2016).

1.2 N-BODY NUMERICAL INTEGRATION: THE TRADES CODE

The determination of the mass and orbital parameters of exoplanets from observational data is a difficult inverse problem. In order to solve it, I used the software TRADES (TRAnsits and Dynamics of Exoplanetary Systems). The code is based on a numerical N-body approach, which is conceptually simpler than the analytical one based on the perturbation theory, but computationally more intensive. TRADES simulates the dynamics of exoplanetary systems and it simultaneously reproduces the observed mid-transit times (T_0s) and RVs (Borsato et al., 2014).

1.2.1 The algorithm

TRADES is a computer program originally developed in Fortran 90 (parallelized with openMP) and now available also in Python. To solve the inverse problem, TRADES can be run in different modes and in each mode the program integrates the orbits, calculates the T_0s and the RVs, and compares them with the observed ones, searching for the solution with the lowest residuals. TRADES computes the orbits using a Runge-Kutta-Cash-Karp integrator (RKCK, Cash & Karp 1990). Compared to a sympletic integrator, that numerically solves the Hamilton's equations by preserving the Poincarè invariants, the RKCK integrator conserves the total angular momentum and the total energy, and it uses small and variable steps to maintain the numerical precision during the integration. These features make it fast, but not suitable for long-term time integrations.
The TRADES modes in the Fortran 90 version are:

- **Integration**: it runs an integration of the planetary orbits. If provided, it compares the observed T_0s and RVs with the simulated ones and it returns $\chi^2_r = \chi^2/dof$, with dof= degrees of freedom.

- **Grid search**: it samples the orbital elements of a perturbing body. The sampling spacing can be chosen by setting the number of steps, or the step size, or a number of points chosen randomly within the parameter bounds. For any given set of values, the orbits are integrated and the observed T_0 and RVs are compared with the simulated ones. At the end of the integration, the Levenberg-Marquardt (LM) algorithm can be called for each combination of the parameters.

- **Levenberg-Marquardt (LM) algorithm**: it exploits the Levenberg-Marquardt minimization method to find the solution with the lowest residuals (minimum χ^2_r). An initial guess on the orbital parameters of the

perturbers is required and it could be provided by the grid search method.

- **Genetic algorithm (GA)**: it searches for the best orbit performing a genetic optimization (Goldberg, 1989). Compared to other optimizers, the GA algorithm is slow; however, if a global solution exists, it should always converge after the appropriate number of iterations. In TRADES, the PIKAIA implementation is used (Charbonneau, 1995).

- **Particle Swarm optimization** (**PSO**, Tada 2007): it searches for the global solution of the problem using an optimization mechanism inspired by the social behaviour of bird flock and fish school (Eberhart, 2007).

- **PolyChord** (**PC**, Handley et al. 2015): it is a nested sampling algorithm tailored for high dimensional parameter spaces, based on a Bayesian approach. It uses a slice sampling at each iteration to sample within the hard likelihood constraints of nested sampling.

Let us briefly point out the advantages of each approach. The grid search is suitable to explore a limited subset of the parameter space, or to analyze the behavior of the system by varying only some parameters (e.g. to investigate the effect caused by a perturber with different masses). In fact, even though all the parameters are allowed to be sampled in the grid, the number of simulations increases hugely as the number of parameters increases and so does the computational time. In a wider parameters space, GA and PSO algorithms are more appropriate. Note that the orbital solutions found with these algorithms can eventually be refined using the LM mode. Narrower parameters boundaries are preferable also for the PC mode (see Handley et al., 2015). An advantage of the PC mode consists in the fact that it can semi-independently identify and evolve separate modes of a posterior distribution.

In the Python version, TRADES can perform a Bayesian analysis, starting from the solutions obtained with the global exploration of the parameter space, using the emcee package (Foreman-Mackey et al., 2013), an affine invariant MCMC ensemble sampler (Goodman & Weare, 2010).

1.2.2 Mathematical implementation

The integration of the orbits is performed in the (X, Y, Z) reference frame, where the $X - Y$ plane corresponds to plane of the sky and the Z axis points to the observer. Given the initial orbital elements, the first step is

the calculation of the state vectors $\boldsymbol{r}$ and $\dot{\boldsymbol{r}}$ in the orbital plane (x, y, z) (see Murray & Dermott, 2000):

$$\begin{aligned} \boldsymbol{r} &= \begin{pmatrix} x \\ y \\ z \end{pmatrix} = \begin{pmatrix} a(\cos E - e) \\ a\sqrt{1-e^2}\sin E \\ 0 \end{pmatrix}, \\ \dot{\boldsymbol{r}} &= \begin{pmatrix} x \\ y \\ z \end{pmatrix} = \begin{pmatrix} \frac{n}{1-e\cos E}(-a\sin E) \\ \frac{n}{1-e\cos E}(a\sqrt{1-e^2}\cos E \\ 0 \end{pmatrix}, \end{aligned} \tag{14}$$

where $n = 2\pi/P$ and E is the eccentric anomaly, that is obtained solving with the Newton-Rhapson method the Kepler's equation $\mathcal{M} = E - e\sin E$. The second step is the transformation of the state vectors from the orbital plane to the reference plane of the observer, by applying three consecutive transposed rotation matrices:

$$\begin{pmatrix} X \\ Y \\ Z \end{pmatrix} = R_3^T(\Omega) R_1^T(i) R_3^T(\omega) \begin{pmatrix} x \\ y \\ z \end{pmatrix}, \tag{15}$$

where $R_l(\phi)$ indicates a rotation matrix with rotation angle ϕ and rotation axis l (where $l = \{1, 2, 3\} = \{x, y, z\}$).
The third step is the integration, starting from the initial state vectors, of the astrocentric equation of motion of planet k (Murray & Dermott, 2000)

$$\ddot{\boldsymbol{r}}_{\boldsymbol{k}} = -G(m_0 + m_k)\frac{\boldsymbol{r}_{\boldsymbol{k}}}{r_k^3} + G\sum_{\substack{j=2 \\ j,k}}^{N} m_j\left(\frac{\boldsymbol{r}_{\boldsymbol{j}} - \boldsymbol{r}_{\boldsymbol{k}}}{|\boldsymbol{r}_{\boldsymbol{j}} - \boldsymbol{r}_{\boldsymbol{k}}|^3} - \frac{\boldsymbol{r}_{\boldsymbol{j}}}{r_j^3}\right), \tag{16}$$

where m_0 is the mass of the star and N is the number of the bodies in the system. The first term of equation 16 represents the gravitational attraction of the star, while the second term is the gravitational force due to the mutual interactions with other bodies. During the integration, the semi-major axis is constrained between a minimum ($a_{\min}$) and a maximum ($a_{\max}$) value. The lower limit corresponds to the stellar radius, while the maximum limit is equal to five times the largest semi-major axis of the system. Furthermore, the minimum allowed distance between two planets is set at the Hill's sphere radius (Murray & Dermott, 2000). When one of these constraints is violated, the integration stops and the combination of the parameters is rejected.

Finally, to compute the transit times, `TRADES` considers the condition of an eclipse, that happens when the sign of the X or Y coordinate changes between two consecutive steps of a planet's trajectory. Then, the roots of the

sky-projected separation are seeked with the Newton-Rhapson method, by solving $g(\boldsymbol{r}_k, \dot{\boldsymbol{r}}_k) = \boldsymbol{r}_k \cdot \dot{\boldsymbol{r}}_k = 0$, and moving and iterating by the quantity

$$\delta t = -g\left(\frac{\partial g}{\partial t}\right)^{-1}. \tag{17}$$

In this way, the accuracy of the mid-transit time and of the corresponding state vector ($\boldsymbol{r}_{\mathbf{mid}}$, $\dot{\boldsymbol{r}}_{\mathbf{mid}}$) is equal to δt: in TRADES, this value is set at the machine precision. In the following step, a comparison between the projected sky separation at the transit time ($|\boldsymbol{r}_{\mathbf{s,mid}}|$) and the planetary and stellar radii (R_k, $R_\star$) allows to determine the presence of four contact times (transit), two contact times (grazing eclipse), or no transit (Fabrycky, 2010) – again at the machine precision. Differently from Borsato et al. (2014), the current TRADES version does not assume constant orbital elements around T_0, but it uses exactly the same integration method described in Fabrycky (2010). As final step, the program corrects each contact point and T_0 for the light-time travel effect due to the motion of the star around the barycenter of the system (barycentric correction).

2 | TARGET SELECTION

In order to perform a TTV analysis, a suitable target is required: a multiple planetary system, with at least two transiting planets showing a strong, anti-correlated TTV signal. Moreover, since the purpose of this work is the characterization of a not previously analyzed system, I searched for a candidate that had not been studied in details by other authors.
The selected target was the planetary system *Kepler*-279 (KOI-1236).

2.1 THE HOLCZER CATALOG: *Kepler* CANDIDATES WITH TTV SIGNAL

The starting point for the search of an appropriate target was the exoplanetary catalog of Holczer et al. (2016), available at `http://vizier.cfa.harvard.edu/viz-bin/VizieR?-source=J/ApJS/225/9`. It is a transit timing catalog of 2599 *Kepler* Objects of Interest (KOIs), based on short (1-min) and long (30-min) cadence light curves of the full seventeen quarters of the *Kepler* mission.[1] The catalog is meant to be used for the study of *Kepler* multiple-planet systems that show TTV signal. The TTV data could also help in constructing a statistical picture of the architecture and frequency of the KOIs multiple planetary systems.
Let us briefly summarize the steps for the catalog's production (for details, see Holczer et al. 2016). The authors started with the list of 4960 KOIs in the NASA Exoplanet Archive (`http://exoplanetarchive.ipac.caltech.edu`), as of 23/11/2013. They excluded the KOIs listed as false positive and the ones for which one of the following statements was true:

- The folded light curve did not display a significant transit, either if the signal-to-noise ratio (SNR) was < 7.1 or if p-value of the transit model exceeded 10^{-4}.

- The transit depth was larger than 10%, since the object was labelled as an eclipsing binary, or the KOI was already listed in the Villanova eclipsing binary catalog (`http://keplerebs.villanova.edu/`).

[1] During the four years of the mission, the spacecraft completed a 90° roll every 3 months to optimize solar panel efficiency. Therefore, the operations are divided into four quarters each year, separated by the quarterly rolls of the spacecraft, for a total of seventeen quarters.

- The orbital period was larger that 300 days, because there would be too few transits for a significant TTV analysis.

For the 2599 KOIs left from the previous selection, they detrended and folded the *Kepler* long-cadence data, using the ephemeris of the NASA Exoplanet Archive, in order to obtain a good template for the transit. They used three different templates to fit the transit: a Mandel & Agol (2002), a Legendre polynomial, and a Fermi function template model. The first one was preferred whenever it had given a good enough fit, because of its astrophysical basis. The following step was the determination of the mid-transit time (T_0s): in order to derive the timing of a specific transit, they searched through a grid of timings around the expected T_0s, fitting the data with the transit model for each time shift. At the end of the grid-search, the point with the lowest χ^2 was the first guess for the transit time. Then, a finer search was performed using MATLAB's FMINSEARCH function, allowing the duration of the transit to vary for the KOIs with a transit duration > 1.5 hours (calculated from the initial fit) and SNR>10. As final step, they derived the $O-C$ as the difference between the measured T_0 and the expected time, based on a linear ephemeris.

In order to identify KOIs with significant TTV modulation, they selected the objects with more than six transit measurements and they computed a few statistics on their $O-C$ series:

- the modified χ^2 of the $O-C$ series[2] and the p-value against no-variation assumption: low p-values due to high values of σ_{o-c} relatively to $\bar{\sigma}_{t_0}$ might indicate a significant TTV;
- the power spectrum of the periodogram of the $O-C$ series and the p-value assigned to the periodicity corresponding to the highest peak in the periodogram;
- an alarm score $\mathcal{A}$ of the $O-C$ series (Tamuz et al., 2006) and the associated false-alarm probability, calculated counting the number of permutation with $\mathcal{A}$ higher than the peak of the real data, over a total of 10^4 random permutations;
- a long-term polynomial fit to the $O-C$ series, with degree lower than four and its significance through an $\mathcal{F}$-test.

If any of the aforementioned statistics returned a p-value < 10^{-4}, the analyzed KOI was considered having a significant TTV modulation. KOIs

[2] The modified ratio $\sigma_{o-c}/(1.48\bar{\sigma}_{t_0})$, squared and multiplied by the number of measurements, gives the modified χ^2, where σ_{o-c} is the scatter of the $O-C$s (defined as 1.4826 times the median absolute deviation of the $O-C$ series) and $\bar{\sigma}_{t_0}$ is the median of the timing uncertainties.

showing TTV modulations with P>100 days were classified as objects having a significant long-term TTV: Table 5 in Holczer et al. (2016) lists the 260 KOIs of this type. Ten additional systems with significant short-term TTV (period in range 3-80 days) are listed in Holczer et al. (2016) – Table 7. For all these 270 systems, either a periodic cosine function or a parabola[3] were fitted to the data, in order to find TTV periods and amplitudes. In the case of a parabolic fit, only an estimate for the amplitude was possible: it was calculated as half the difference between the maximum and minimum values of the parabola.

2.1.1 Selection criteria

In order to select a suitable target for my TTV analysis, I based my search on the list of the 270 *Kepler* candidates with significant TTV modulations in the Holczer catalog. As a first step, I selected the systems with:

- Co-sinusoidal fit: I excluded KOIs with a parabolic $O-C$ fit, since in that case it is not possible to determine period and amplitude of the TTV signal.
- At least two transiting exoplanets: systems with more that one planet showing a strong TTV signal are easier to analyze, while the signal from a single transiting planet is extremely difficult to interpret (see Sec. 1.1). Therefore, I considered only planetary systems with multiplicity ≥ 2 and at least two planets showing transit and strong TTV signal.

For the 32 systems left, I searched in literature for specific works on any of them, excluding any system with a published analysis: I did not want to analyze an already characterized object. Note that I did not consider the validation papers of a big number of planets as a *specific* work, since they usually rely on statistical and automatic procedures that can only give, when calculated, an upper limit or an approximate mass value (e.g. Ford et al. 2012; Rowe et al. 2014; Xie 2014). Moreover, if a specific paper was present, but the authors could not constrain the mass or could only calculate an upper limit, I did not exclude the system, as I could improve the characterization of the system with my work, searching for a mass value. I found 7 systems that matched these criteria (Table 1). For all of them, I plotted the $O-C$ diagram, looking for the best anti-correlated signal and for the system with the most interesting properties. My final choice was the planetary system *Kepler*-279 (KOI-1236), since it has four transiting planets, two of which show an anti-correlated signal (Fig. 7).

[3] A parabolic fit means that the time-scale of the modulation is longer than the observational baseline.

Table 1: *Kepler* systems with at least two transiting planets showing a significant TTV signal and no previous specific works in literature.

Name	Multiplicity[a]	TTV planets[b]
Kepler-396	2	c,d
Kepler-23	3	c,d
Kepler-54	3	b,c
Kepler-176	3	c,d
Kepler-49	4	b,c
Kepler-279	4	c,d
Kepler-55	5	b,c

Note – [a] Total number of planets in the system, including candidates. [b] Planets in the system showing a significant TTV signal.

2.2 THE *Kepler*-279 SYSTEM

Kepler-279 (KOI-1236) is an F-type star (for details about stellar parameters, see Section 2.2.3) hosting three confirmed planets and one planetary candidate, KOI-1236.04. The planetary parameters retrieved from the NASA Exoplanet Archive are listed in Table 2.

Table 2: Planetary parameters of the *Kepler*-279 system.

Kepler name	KOI	Period [day]	Radius [$R_\oplus$]	Mass [$M_\oplus$]
Kepler-279b	1236.02	12.30971 ± 0.00004	$3.68^{+1.04}_{-0.75}$	–
Kepler-279c	1236.01	35.73557 ± 0.00011	$5.61^{+1.25}_{-0.93}$	$49.4^{+7.2}_{-5.9}$
Kepler-279d	1236.03	54.42054 ± 0.00028	$4.76^{+1.33}_{-0.99}$	$37.5^{+5.5}_{-4.5}$
–	1236.04	98.35315 ± 0.00179	$4.13^{+0.69}_{-0.92}$	–

Note – Period and radius of the three confirmed planets are taken from Morton et al. (2016). Period and radius of KOI-1236.04 are taken from the *Kepler* Pipeline, since there are no validation papers in literature. Planetary masses are calculated statistically in Xie (2014).

The system shows period commensurabilities suggesting a, or close to, resonant configuration, where planets b and c are close to a 3:1 MMR, c and d are close to a 3:2 MMR, and KOI-1236.04 and d are close to a 2:1 MMR. The first order resonance of planets c,d explains the observed strong, anti-correlated TTV signal; on the other hand, *Kepler*-279b is not included in the Holczer list of 270 objects showing a significant TTV signal. The $O - C$ series of the three confirmed planets are shown in Figure 7. In order to

identify possible outliers in the $O-C$ series, I decided to perform a light curve analysis, that was also necessary to confirm or exclude the presence of the fourth planet in the system and, in case, to calculate its $O-C$ series. In fact, the planetary candidate KOI-1236.04 had not been analyzed by Holczer et al. (2016), because its transit features did not match their selection criteria.

2.2.1 Light curve analysis

I used the *Kepler*-279 light curves stored in the *Kepler* mission page at the Mikulski Archive for Space Telescopes (MAST), a NASA funded project to support and provide to the astronomical community a variety of astronomical data archives (`https://archive.stsci.edu/Kepler/data_search/search.php`). Light curve files contain columns with flux information: in particular, the simple aperture photometry (SAP) flux and its uncertainties, and the Pre-search Data Conditioning (PDCSAP) flux, that is the SAP flux corrected by the systematic artifacts (Smith et al., 2012). *Kepler* long cadence light curves (LLC) are stored in 17 quarters, each of them spanning three months, while short cadence light curves (SLC) are divided in quarters that span a month. In each file, I normalized the PDCSAP flux dividing by the median value and I joined all the quarters to obtain the complete light curve, for both long and short cadence data (Fig. 8.)

I used the obtained light curves to check the transits of the three confirmed planets, in order to identify anomalous features that could have influenced the accuracy in the $O-C$ series determination. *Kepler*-279b does not show a TTV signal, so it is difficult to recognize an $O-C$ pattern. The data points are spread almost randomly around the zero value. The phase-folded light curve (Fig. 12) shows a less evident transit than those of planets c,d, and this fact could have precluded a precise determination of the mid-transit times in Holczer et al. (2016), yielding to the observed spread in the $O-C$ plot. I checked on the light curve the four transits with the highest scatter:

- 7-th transit ($T_0 = 92.84253$ days[4]): in the light curves, both LLC and SLC, there are no data around T_0. The expected transit time is located exactly in a small gap of the observations. The Holczer et al. (2016) automatic procedure could not have fitted the transit in a proper way, so the T_0 is not reliable: I removed the transit time from the list.

- 33-rd transit ($T_0 = 413.16451$ days): it overlaps the 11-th transit of *Kepler*-279c ($T_0 = 413.3746$ days). As Figure 9 shows, it is difficult to locate the mid-transit time, and the T_0 calculated automatically by Holczer et al. (2016) could be inaccurate, so I discarded the transit.

[4] All the T_0s are referred to BJD – 2454963.875 days.

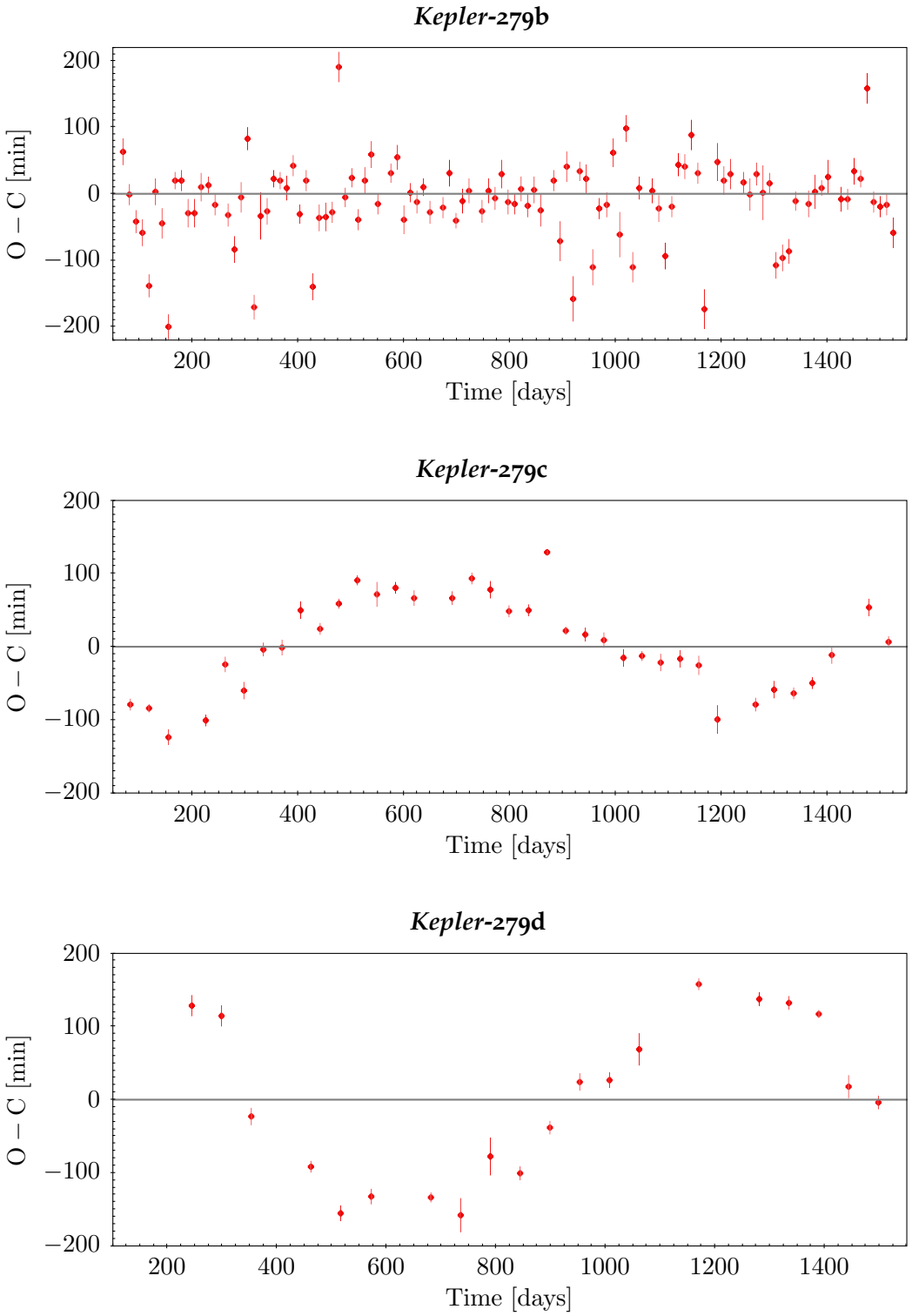

Figure 7: $O - C$ diagram of *Kepler*-279b, *Kepler*-279c, and *Kepler*-279d. Planets c,d show a strong, anti-correlated TTV signal.

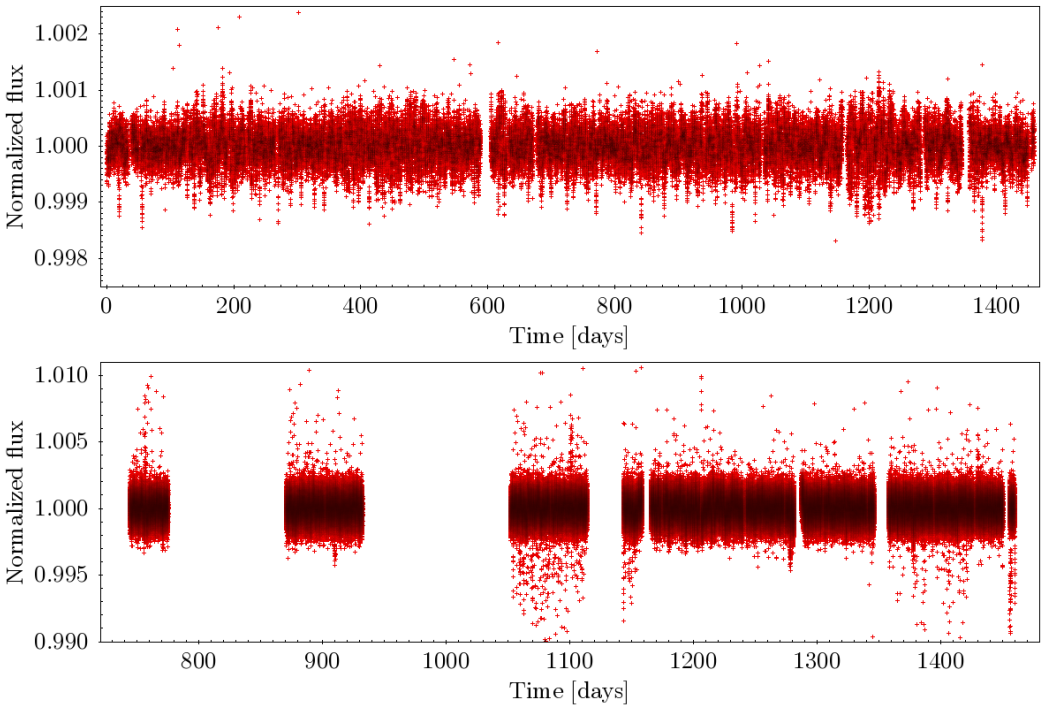

Figure 8: LLC (top panel) and SLC (bottom panel) of *Kepler*-279. Time is referred to the *Kepler* starting date (BJD – 2454963.875 days, BJD=Barycentric Julian Date).

- 89-th ($T_0 = 1102.25340$ days) and 114-th ($T_0 = 1410.22471$ days) transits: the light curve did not display any anomalous features, so I did not discarded the transits. However, as Figure 10 shows, in none of the cases there was evidence of transit (by visual inspection) around the expected transit time, so it is possible that the automatic procedure performed by Holczer et al. (2016) has provided slightly inaccurate transit times, since it was not possible to precisely locate the center of the transit.

Since *Kepler*-279c shows a clear TTV signal, I checked all the transits on the light curve, and I rejected two of them:

- 22-nd transit ($T_0 = 806.50052$ days): in the light curves, both LLC and SLC, there are no data around T_0. The expected transit time is located exactly in a small gap of the observations, so I discarded the transit, as for the *Kepler*-279b case.

- 38-th transit ($T_0 = 1378.33021$ days): it overlaps the 25-th transit of *Kepler*-279d ($T_0 = 1378.2981$ days), as Fig. 11 shows. As for *Kepler*-279b 33-rd transit, I did not consider it in the next simulations.

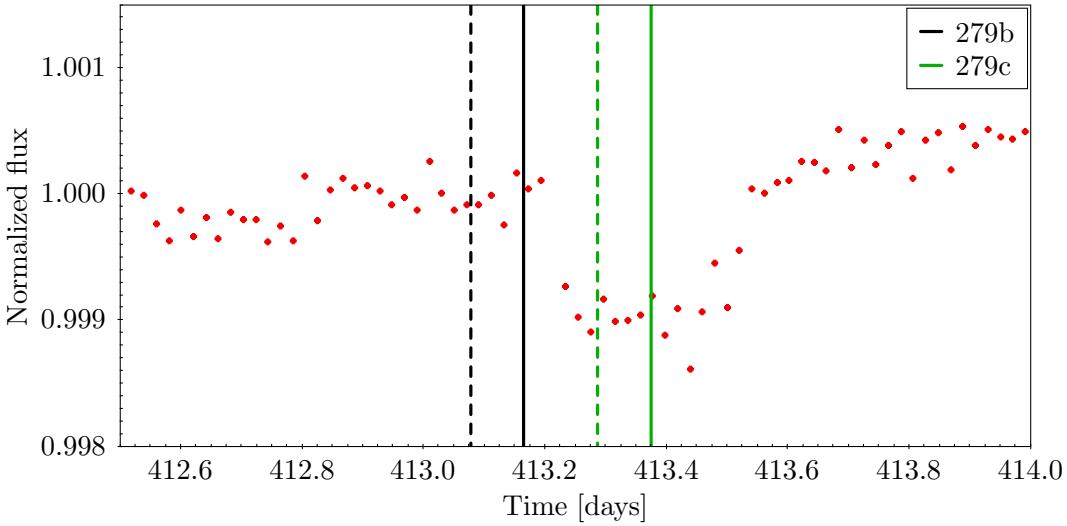

Figure 9: LLC of *Kepler*-279, showing the overlap between the 33-rd transit of *Kepler*-279b (black lines) and the 11-th transit of *Kepler*-279c (green lines). The continuous lines indicate the observed T_0s, while the dashed lines show the time of the ephemeris.

As for *Kepler*-279c, I checked all *Kepler*-279d transits, but I did not identify any anomalous feature, so I did not discard any of the transits from the $O - C$ series.

I also used the LLC and SLC to test the hypothesis of a fourth planet. In fact, the validation report of *Kepler*-279 includes a planetary candidate, KOI-1236.04, which is still not validated from other works: none of the papers regarding the *Kepler*-279 system reports a significant transit signal (Rowe et al., 2014; Xie, 2014; Morton et al., 2016; Hadden & Lithwick, 2017). I performed the phase-folding of the SLC at the orbital period of KOI-1236.04, in order to define more clearly the transit. The phase ϕ is calculated as

$$\phi = \frac{[(t - t_{\rm ref}) \bmod P]}{P}, \tag{18}$$

where mod represents the modulo operation[5], t is the time, P is the period of the transiting planet and $t_{\rm ref}$ is the reference time. I chose as reference time $t_{\rm ref} = T_1 - P/2$, where T_1 is the mid-transit time of the first observed transit, as calculated in Holczer et al. (2016). In this way, since $\phi \in [0, 1]$, the center of the transit after the phase-folding is located at $\phi = 0.5$.
In order to make the transit more evident, I binned the folded SLC in phase with the VARTOOLS program, a command line utility that provides tools for processing and analyzing astronomical time series data (Hartman & Bakos, 2016). I set the binsize=0.001, taking the median of points in a bin and setting the time at the center of the bin as output time for each bin.

[5] The modulo operation finds the remainder after the division of one number by another.

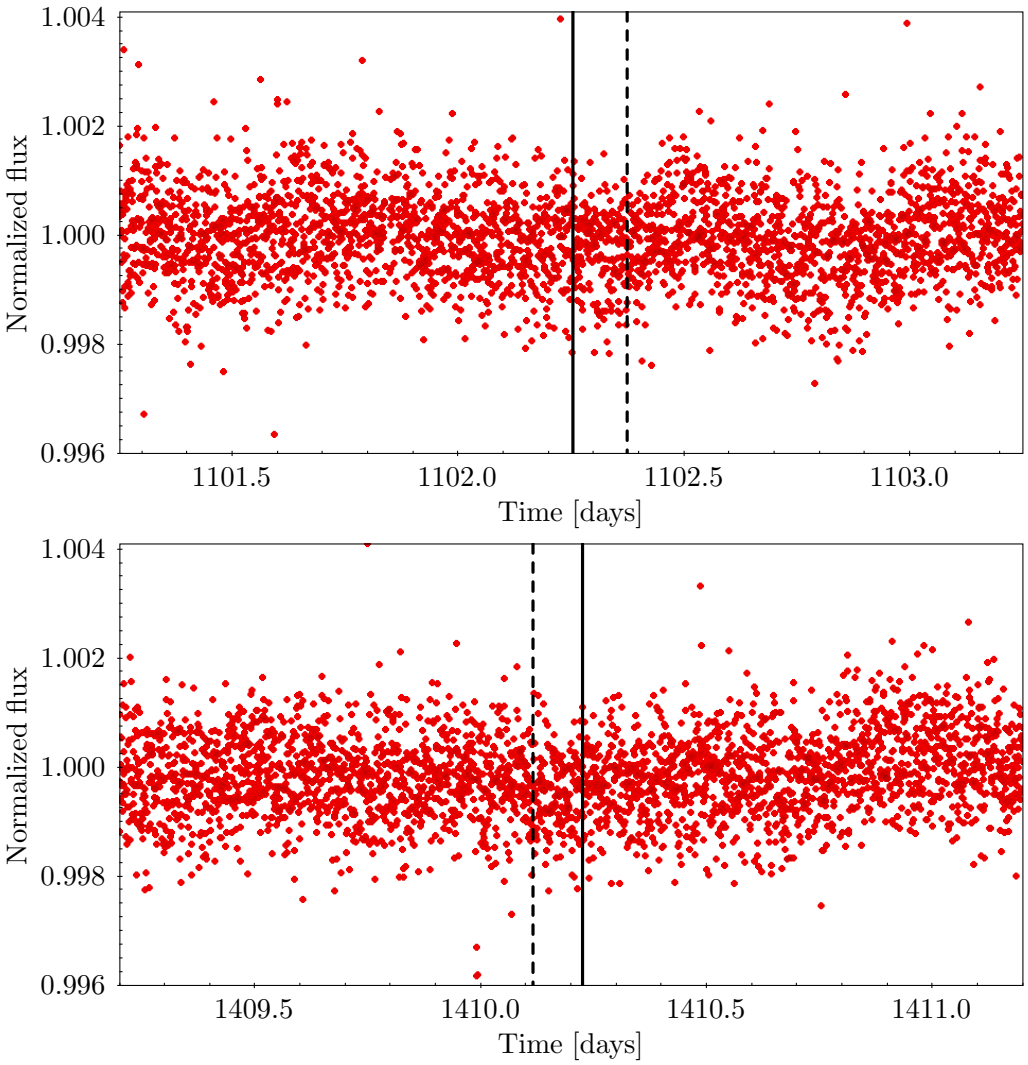

Figure 10: SLC of *Kepler*-279, showing the 89-th (top panel) and the 114-th (bottom panel) transit of *Kepler*-279b. The continuous black line indicates the observed T_0s, while the dashed line show the time of the ephemeris.

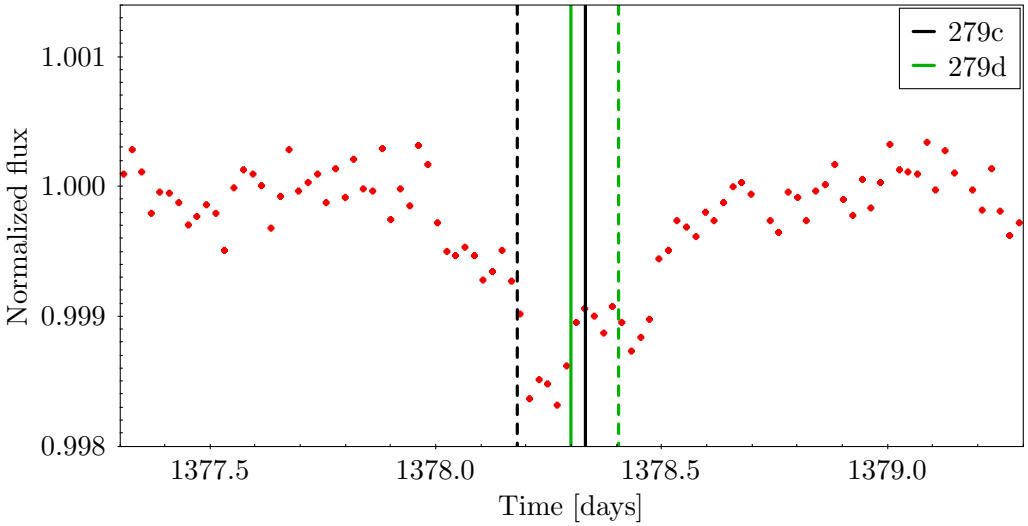

Figure 11: Same as Fig. 9, but showing the overlap between the 38-th transit of *Kepler*-279c (black lines) and the 25-th transit of *Kepler*-279d (green lines).

Figure 12 shows the phase-folded SLC at KOI-1236.04 period, and the superimposed binned light curve. I used the duration of the transit (Table 3) to stress the ingress and egress moments, but the transit is difficult to identity by visual inspection.

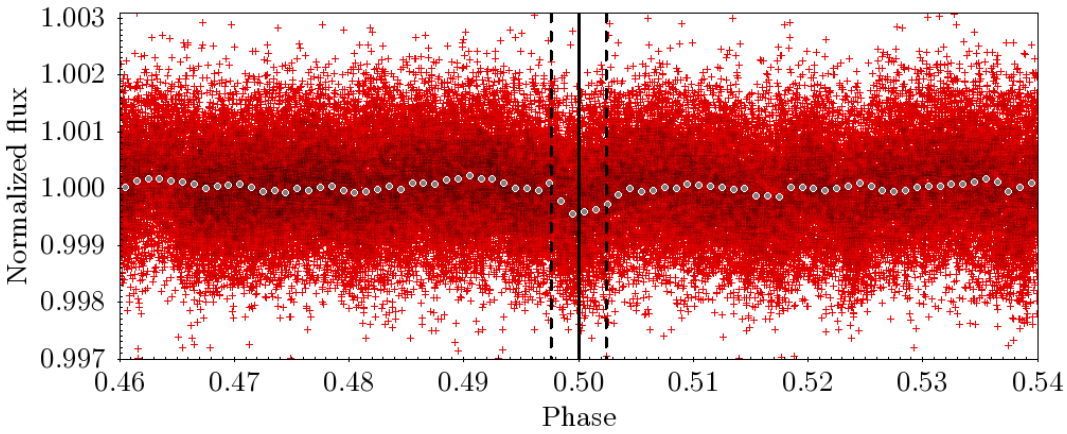

Figure 12: Phase-folded SLC (red crosses) at KOI-1236.04 period; the binned SLC with binsize=0.001 is superimposed (circles). The vertical black line indicates the predicted center of the transit, while the two dashed lines correspond respectively to the beginning and to the end of the transit.

For comparison, I plotted the phase-folded and binned SLC of the three confirmed planets (Fig. 13), all showing a more evident transit.

Since the analysis of the light curve did not show any evidence of transit with KOI-1236.04 period ($P_{\rm KOI}$), I proceeded with the analysis of the periodogram using the Box-fitting Least Squares method, searching for a periodic signal corresponding to the transiting candidate.

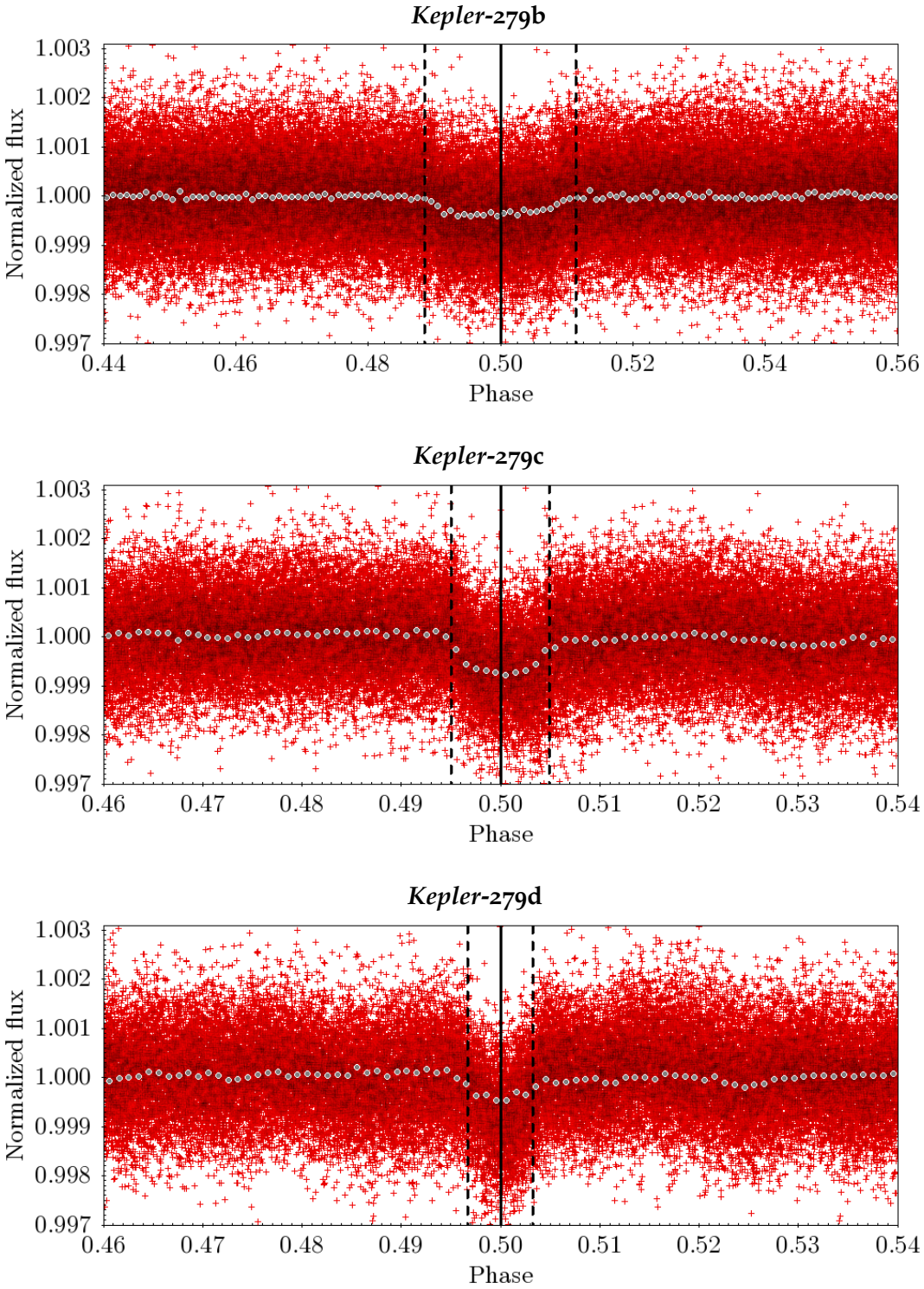

Figure 13: Same as Fig. 12, but for planets *Kepler*-279b, *Kepler*-279c, and *Kepler*-279d.

Table 3: Transit parameters of the *Kepler*-279 system.

Name	$T_{\rm dur}$ [hour][a]	$T_{\rm dur}$ (ϕ)[b]	T_0^c [days]	N_t^d
Kepler-279b	6.289 ± 0.211	0.0228	137.73254 ± 0.01319	112
Kepler-279c	8.995 ± 0.213	0.0099	151.07635 ± 0.00507	36
Kepler-279d	8.559 ± 0.499	0.0065	148.92871 ± 0.00410	23
KOI-1236.04	11.314 ± 0.514	0.0106	217.87128 ± 0.00612	12

Note – [a] The transit duration of the confirmed planets is from Morton et al. (2016), while KOI-1236.04 value is reported only in the *Kepler* validation report. [b] Transit duration in units of phase, calculated as $(T_{\rm dur} \bmod P)/P$. [c] Mid-transit time of the first detected transit (BJD-2454833.0): the values of the confirmed planets are from Holczer et al. (2016), while KOI-1236.04 value is from the *Kepler* validation report. [d] Number of detected transits in the *Kepler* validation report.

2.2.2 Box-fitting Least Squares analysis

The Box-fitting Least Squares (BLS) method is based on a box-fitting algorithm that analyzes stellar photometric time series searching for periodic transits by extrasolar planets (Kovács et al., 2002). The algorithm searches for signals characterized by a periodic alternation between two discrete levels, with much less time spent at the lower level, resulting in a box-shaped transit model[6]. The algorithm is particularly useful where the SNR is small and the signal cannot be identified by monitoring a single transit, because the decrease in the stellar brightness is buried in the noise. The significance of the detection depends primarily on the effective SNR of the transit: Kovács et al. (2002) claims that the effective SNR should exceed a value of 6 in order to get a significant detection.

I converted the flux in magnitudes, then I calculated the magnitude offset of each quarter, and I finally joined the 17 LLCs. I ran iteratively the BLS algorithm implemented in VARTOOLS on the total LLC. The BLS algorithm computes the periodogram of the LLC and it returns the period, the depth, and the duration of the main peak[7], then it subtracts the transit model from the light curve before repeating the BLS search. In this way, once the stronger transit signals are subtracted, it is possible to also identify

[6] Note that the algorithm is suitable only for planets detection: indeed, the box-shape assumption ignores all other features expected in planetary transits, like the gradual ingress and egress phases and the limb-darkening effect. The effectiveness of the algorithm relies precisely on this simplifying assumption, which is justified as long as the interest is a detection.

[7] The VARTOOLS implementation returns the SNR (instead of the power, usually adopted in the Lomb-Scargle periodogram) as a function of the period.

Table 4: Parameters of the first seven iterations of the BLS analysis.

Iteration	Period [d]	T_0^a	SNR	SPN^b	Depth [%]	N$_t^c$
1-st	35.7327	151.1742	14.49	19.86	0.074	38
2-nd	12.3096	137.6841	11.38	17.30	0.041	112
3-rd	54.4223	148.6693	6.40	9.69	0.042	26
4-th	261.2144	334.3957	4.03	8.75	0.020	5
5-th	55.8321	176.04861	4.14	7.57	0.021	23
6-th	60.8073	158.6970	3.91	8.13	0.019	23
7-th	131.4744	228.3227	4.04	7.04	0.025	11

Note – The horizontal line after the third row marks the iterations corresponding to the three confirmed planets. [a] T_0 of the first detected transit (BJD–2454900). [b] Signal-to-Pink Noise. [c] Number of detected transits.

the weaker periods, corresponding to transiting planets with low SNR. The BLS search needs the ranges of some parameters:

- The fraction of orbit in transit: $q \in [0.001 - 0.1]$
- The period to search in: $P \in [10, 300]$ days

I set the number of frequencies to analyze $N_{\rm freq} = 100000$, and the number of the phase bins $N_{\rm bin} = 500$. In order to obtain a refined estimate of the transit time, duration and depth, I exploited the VARTOOLS routine that fits a trapezoidal transit to each BLS peak. I chose to repeat the analysis up to the 7-th iteration, in order to allow the identification of the candidate with faint signal, and to have a comparison with the parameters of non-significant detections. The obtained parameters are listed in Table 4 and the periodograms are shown in Fig. 14 – 20. The parameters obtained from the BLS analysis allow the identification of the main peaks of the first three iterations with the three confirmed planets, respectively *Kepler*-279c, *Kepler*-279b and *Kepler*-279d. The comparison among Table 2, Table 3, and Table 4 shows that periods, T_0s, and number of detected transits are consistent with literature values: the small discrepancies can be explained considering that the BLS analysis can only give rough information regarding the transit features. The BLS search did not find a peak that corresponds to the period of KOI-1236.04; moreover, the peaks of the last four iterations have very low values of SNR, under the threshold of a significant detection according to Kovács et al. (2002). In addition to the SNR, I also considered the

signal-to-pink noise[8] (SPN) as significance estimator. The SPN threshold for significance has to be estimated empirically, because no analytical expression is present in literature. I decided to run the BLS analysis on the inverted light curve, that is a light curve with inverted magnitude sign, after the removal of the three confirmed planets. In this way, if the SNR and the SPN values have the same order of the values obtained from the first analysis, the peaks correspond to statistical fluctuations and there is no transit signal, but only noise. The results of this analysis (Table 5) confirmed that peaks of iterations $\geq$ 4-th do not correspond to a transit signal, but they are related to statistical noise.

Table 5: Parameters of the iterations $\geq$ 4-th in the BLS periodogram of the inverted light curve.

Iteration	Period [d]	T_0^a	SNR	SPN	Depth [%]	N_t^b
4th	162.8515	149.1184	4.73	8.22	0.018	9
5th	174.3813	300.6887	4.00	7.79	0.031	8
6th	289.8297	328.0607	4.11	7.20	0.044	4
7th	132.5356	260.3331	4.24	10.21	0.012	12

Note – [a] T_0 of the first detected transit (BJD–2454900). [b] Number of detected transits.

Thanks to the previous analysis, I rejected the hypothesis of a fourth planet in the *Kepler*-279 system and I associated the signal corresponding to KOI-1236.04 to a False Alarm. Consequently, the TTV analysis in Chapter 3 has been performed assuming a system with three planets.

[8] The pink noise is a signal or a process with a frequency spectrum such that the power spectral density is inversely proportional to the frequency of the signal.

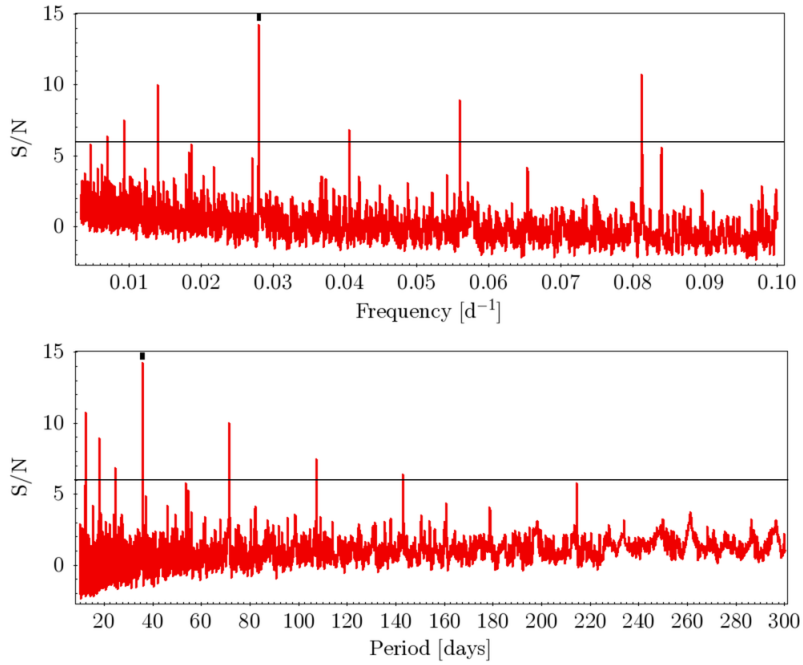

Figure 14: Periodogram obtained from the BLS analysis, showing the main peak of the 1-st iteration (black dash), corresponding to *Kepler*-279c. The y-axis shows the SNR and the horizontal line indicates the threshold for significance of Kovács et al. (2002).

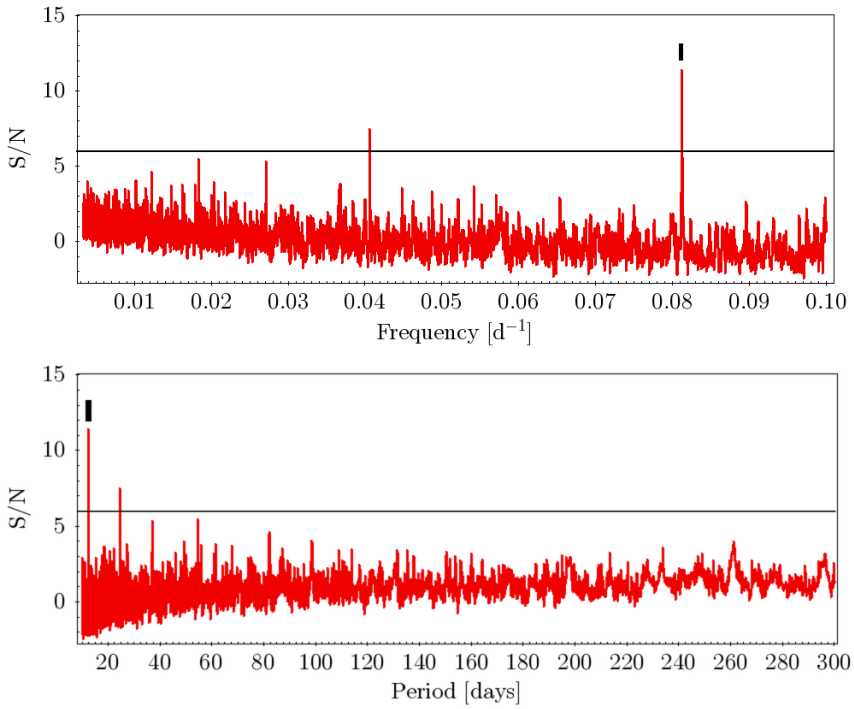

Figure 15: Same as Fig. 14, but for the 2-nd iteration of the BLS, showing the main peak corresponding to *Kepler*-279b.

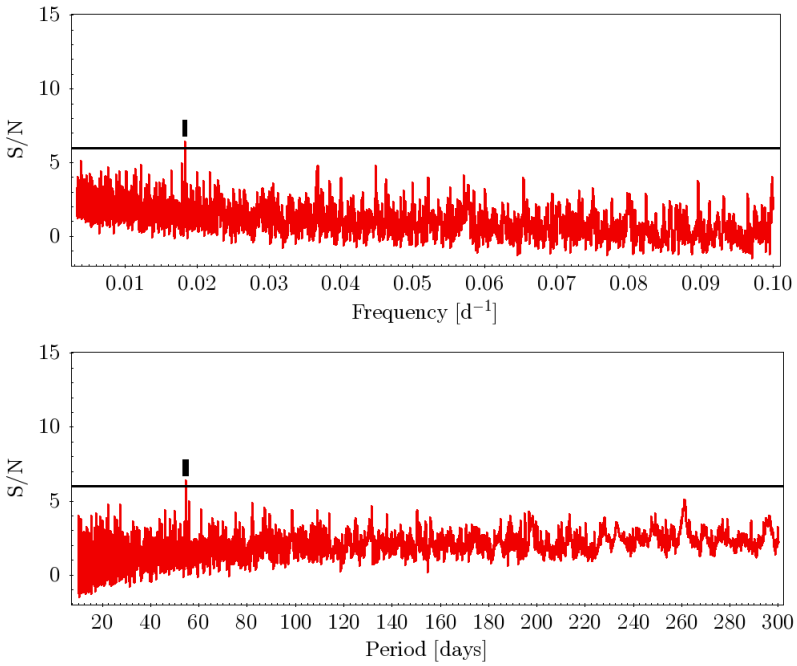

Figure 16: Same as Fig. 14, but for the 3-rd iteration of the BLS, showing the main peak corresponding to *Kepler*-279d.

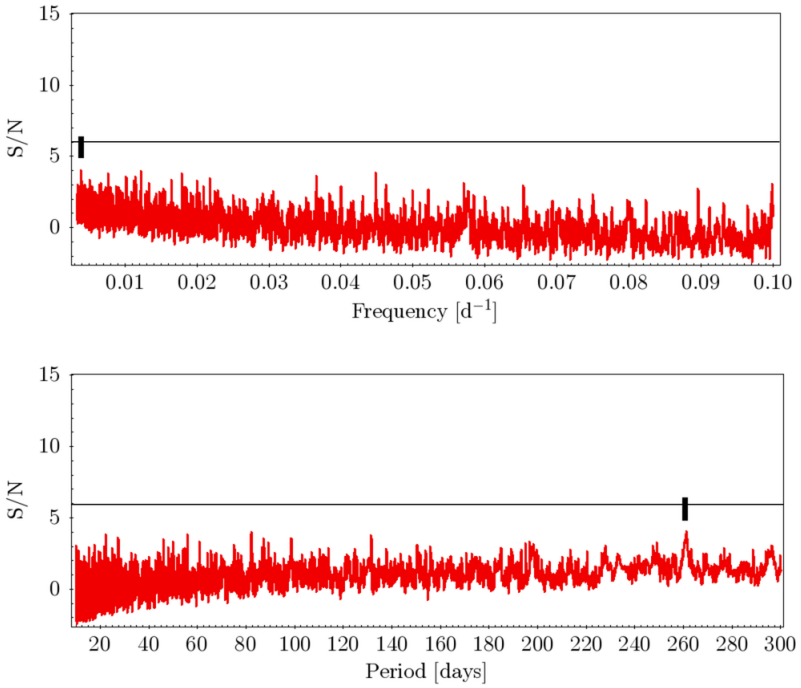

Figure 17: Same as Fig. 14, but for the 4-th iteration of the BLS.

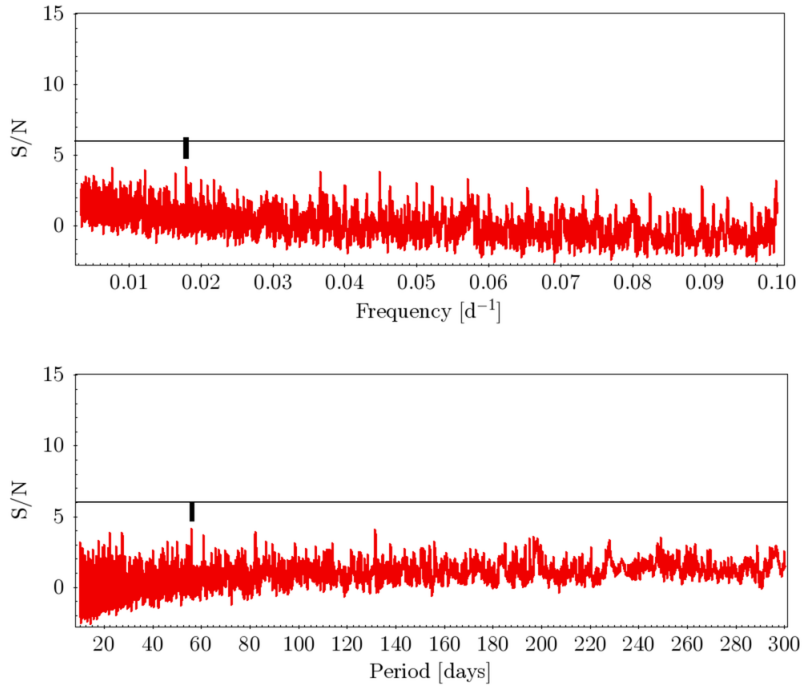

Figure 18: Same as Fig. 14, but for the 5-th iteration of the BLS.

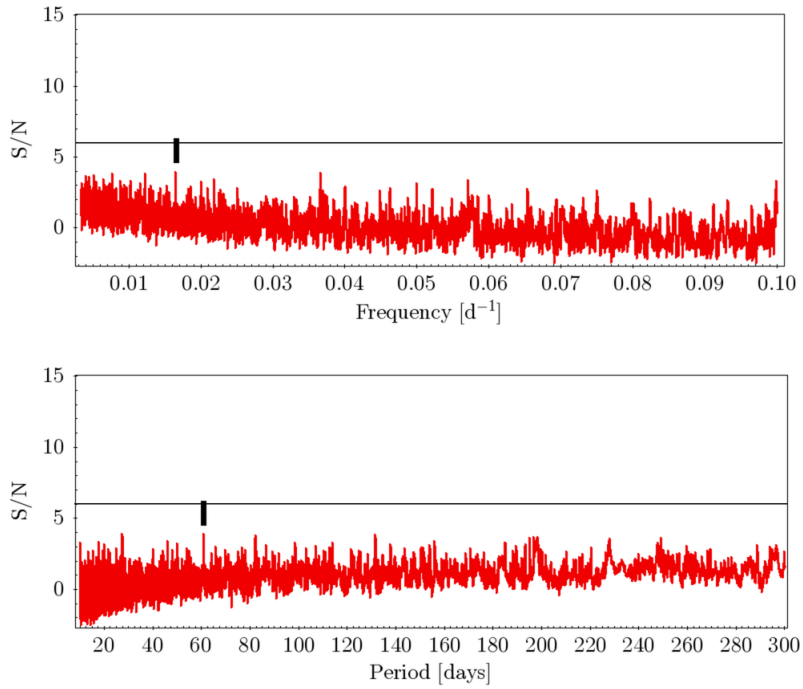

Figure 19: Same as Fig. 14, but for the 6-th iteration of the BLS.

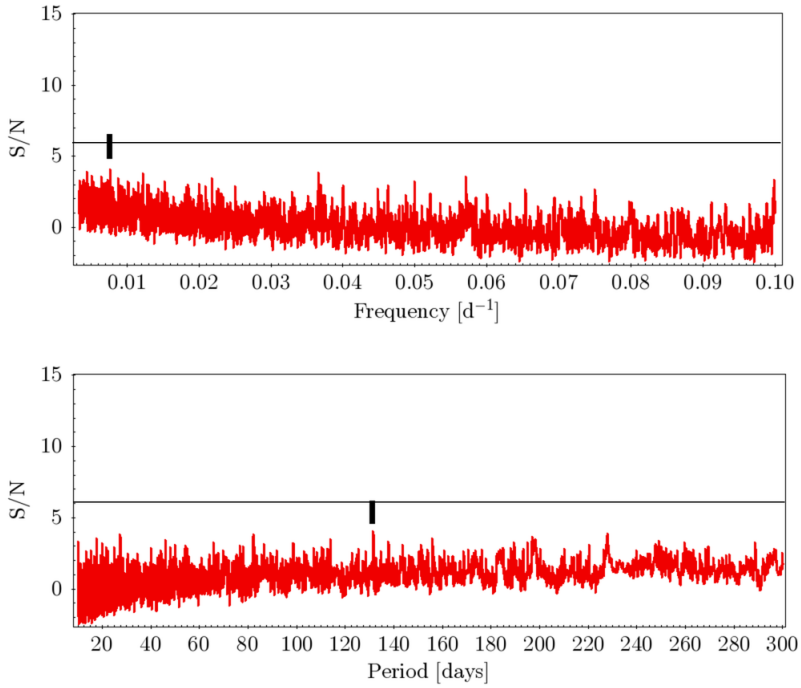

Figure 20: Same as Fig. 14, but for the 7-th iteration of the BLS.

2.2.3 Stellar parameters

Stellar parameters, and in particular mass and radius, are essential to determine planetary properties, since the models depend on relative quantities ($k \equiv R_p/R_\star$ from transits, $M_p/M_\star$ from TTVs, where $R_\star$ and $M_\star$ are the stellar radius and mass, respectively).
Different authors (Rowe et al., 2014; Morton et al., 2016)[9] analyzed the star *Kepler*-279 and found different parameters values. I checked for the consistency of these literature values, in particular $R_\star$, and I included in my analysis the Gaia Data Release 2 (G-DR2)[10] data. Table 6 shows the stellar parameters present in literature, except for the radius, that is treated separately.

In the G-DR2 catalog (`http://vizier.u-strasbg.fr/viz-bin/VizieR-3?-source=I/345/gaia2`), the stellar radius $R_{\star,G}$ is not corrected for extinction: since the extinction correction is necessary for a comparison with other literature values, I calculated the absorption coefficient A_G in the G-band in the following way. First, I estimated the colour excess $E(G_{BP} - G_{BR}) = (G_{BP} - G_{BR}) - (G_{BP} - G_{BR})_0$, where $(G_{BP} - G_{BR}) = 0.6536$ mag is the observed colour index reported in the G-DR2 catalog, and $(G_{BP} - G_{BR})_0 = 0.629$ mag is the intrinsic colour index, that I derived from Rowe et al. (2014) spec-

[9] Rowe et al. (2014) used spectroscopic stellar parameters, while Morton et al. (2016) calculated them fitting the isochrones with the Python module `vespa`.
[10] Released on 25th April 2018 by Gaia Collaboration et al. (2018).

Table 6: *Kepler*-279 stellar parameters.

Source	mag[a]	$T_\star$ [K]	A[b] [mag]	Distance [pc]	$M_\star$ [$M_\odot$]
G-DR2	13.584	6692 ± 260	0.049 ± 0.040	1069.17 ± 22.27	–
Rowe (2014)	–	6363 ± 259	–	–	1.15 ± 0.15
Morton (2016)	–	6488^{+77}_{-67}	$0.04^{+0.05}_{-0.03}$	$1223.000^{+272.393}_{-197.624}$	$1.32^{+0.15}_{-0.11}$
NASA Archive[c]	13.659	6366 ± 116	$0.373^{+0.005}_{-0.015}$	$1157.82^{+181.76}_{-272.64}$	$1.10^{+0.16}_{-0.16}$

Note – [a] Magnitude is in G-band for G-DR2 and in *Kepler* band for the NASA Exoplanet Archive. [b] Absorption coefficient is in Johnson V-band for Morton et al. (2016) and for the NASA Exoplanet Archive. For G-DR2 absorption coefficient, see the text for explanations. [c] NASA Exoplanet Archive values are taken from $Q1-Q17$ $DR25$ (Mathur et al., 2017).

troscopic temperature[11]. Then, I converted $E(G_{BP}-G_{BR}) = 0.0246$ mag in $E(B-V) = 0.0205$ mag, using the conversion coefficients reported in Evans et al. (2018). I calculated the extinction coefficient $A_V = 0.063$ mag using the relation $A_V = R_v\, E(B-V)$, and assuming $R_V = 3.1$. Finally, I derived $A_G = 0.049 \pm 0.040$ mag using the conversion coefficient $A_G/A_V = 0.771$ tabulated in Sanders & Das (2018) –Table A.1. I corrected $R_{\star,G}$ with the calculated A_G (Table 6) using the formula:

$$R_{\star,\mathrm{corr}} = R_{\star,G}\, 10^{(0.2\, A_G)}\,. \tag{19}$$

In addition, I exploited G-DR2 data to calculate *Kepler*-279 radius in a different way: under the black body assumption, once luminosity and temperature are known, $R_\star$ can be calculated from the Stefan-Boltzmann (SB) equation $L = 4\pi R^2 \sigma T^4$ – where L, R, and T are respectively the luminosity, the radius and the temperature of a black body, and σ is the Stefan-Bolzmann constant. In order to obtain the bolometric luminosity L_{bol}, I used the apparent magnitude m_g and the distance d from the G-DR2 catalog (Table 6) to calculate the absolute magnitude $M_G = m_g + 5 - 5\log_{10}(d\,[\mathrm{pc}]) - A_G$. Then, I estimated the bolometric correction $BC_G = 0.0216$ mag following Andrae et al. (2018) procedure, and I obtained the bolometric luminosity:

$$L_{bol} = 10^{[-0.4(M_G + BC_G - M_{bol,\,\odot})]} = 4.23 \pm 0.05\, L_\odot\,, \tag{20}$$

where $M_{bol,\,\odot} = 4.74$ mag is the bolometric magnitude of the Sun. Finally, using the spectroscopic $T_\star$ (Table 6) from Rowe et al. (2014), I obtained:

$$R_{\star,SB} = \sqrt{\frac{L_{bol}}{4\pi\sigma T_\star^4}}\,. \tag{21}$$

[11] The $T_\star$ value in Rowe et al. (2014) is calculated with the SpecMatch fitting (Petigura et al., 2013) using the spectra acquired at the Keck I telescope.

In $R_{\star,\mathrm{corr}}$, $R_{\star,\mathrm{SB}}$ errors calculation, I used the propagation of errors formula[12]: in case of asymmetric uncertainties on the initial quantities, I assumed as standard deviation the highest value between the two asymmetric errors. I compared the two calculated values, $R_{\star,\mathrm{corr}}$ and $R_{\star,\mathrm{SB}}$, with the literature ones (Table 7).

Table 7: *Kepler*-279 radius from this work and from literature.

Source	$R_\star$ $[R_\odot]$
$R_{\star,\mathrm{G}}$	1.30 ± 0.10
$R_{\star,\mathrm{corr}}$	1.32 ± 0.12
$R_{\star,\mathrm{SB}}$	1.52 ± 0.13
Rowe (2014)	1.746 ± 0.315
Morton (2016)	1.66 ± 0.30
NASA Archive	1.697 ± 0.380

Since all the values agree within the error bars (Fig. 21), I decided to adopt, for the dynamical analysis in Chapter 3, the stellar radius that I calculated using the Stefan-Boltzmann equation, $R_{\star,\mathrm{SB}}$. I calculated the

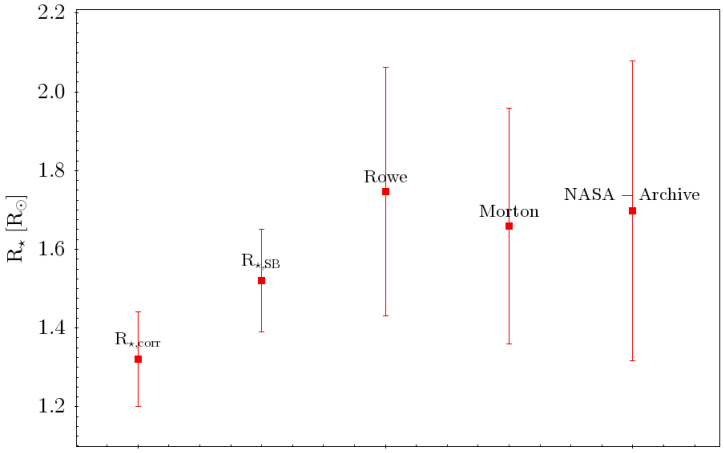

Figure 21: Comparison between *Kepler*-279 radius from literature and from this work. $R_{\star,\mathrm{G}}$ is not shown, because extinction correction is essential for a comparison.

radii of the three confirmed planets using $R_{\star,\mathrm{SB}}$ and Morton et al. (2016)

[12] If $f \equiv f(x_1, \ldots, x_i)_{i=1\ldots N}$ and σ_i=standard deviations of the N variables x_i, the standard deviation σ_f of $f(x_i)$ can be calculated as $\sigma_f = \sqrt{\sum_{i=1}^{N} \left|\frac{\partial f}{\partial x_i}\right|^2 \sigma_i^2}$.

planetary-to stellar ratio k; from now on I will refer to these values as $R_{p,SB}$. I compared $R_{p,SB}$ with the literature values (Table 8), and I included in the comparison also the values of the radii of planets c and d from Xie (2014), determined from the statistical study of the TTV of 15 objects. All the values

Table 8: *Kepler*-279 planetary radii [$R_\oplus$] from literature and from this work.

	Kepler-279b	*Kepler*-279c	*Kepler*-279d
k	$0.021209^{+0.000012}_{-0.002958}$	$0.030659^{+0.000211}_{-0.000872}$	$0.027453^{+0.000287}_{-0.000412}$
$R^a_{p,SB}$ [$R_\oplus$]	3.51 ± 0.79	5.08 ± 0.58	4.55 ± 0.46
Morton (2016)	$3.68^{+1.04}_{-0.75}$	$5.61^{+1.25}_{-0.93}$	$4.76^{+1.33}_{-0.99}$
Rowe (2014)	3.62 ± 0.71	5.34 ± 0.99	4.96 ± 0.97
Xie (2014)^b	–	$4.30^{+1.72}_{-0.41}$	$3.10^{+1.24}_{-0.30}$

Note – [a] Calculated using $R_{\star,SB}$ and Morton et al. (2016) k value. [b] Xie (2014) did not report a value for *Kepler*-279b.

agree within the error bars, as we can see in Figure 22. However, note that both values of planetary radius from Xie (2014) are lower than the others: in fact, the author adopted the stellar properties of the revised Q1-Q16 *Kepler* catalog, that does not consider all *Kepler* quarters, and the stellar radius ($R_\star = 1.07^{+0.43}_{-0.10}$) is considerable lower with respect to all the other literature values (Table 7).
For consistency, since I decided to adopt $R_{\star,SB}$ as stellar radius, I assumed $R_{p,SB}$ values for planetary radii in the dynamical analysis in Chapter 3.

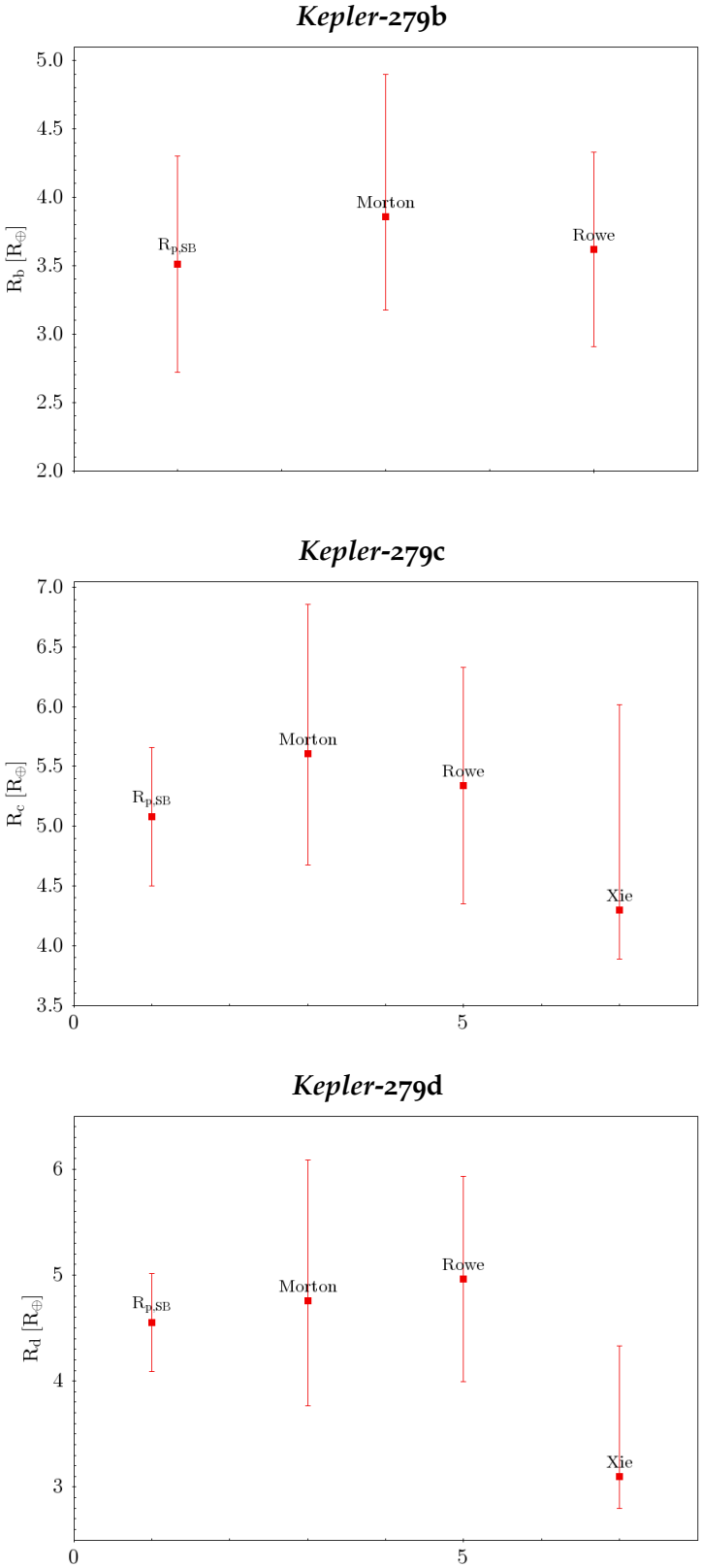

Figure 22: Comparison between planetary radii of the *Kepler*-279 system from literature and from this work ($R_{p,SB}$).

3 DYNAMICAL ANALYSIS

I determined in Chapter 2 that *Kepler*-279 hosts three Neptune-like planets, two of them – *Kepler*-279c and *Kepler*-279d – showing a strong, anti-correlated TTV signal. In order to determine planetary masses and orbital parameters of the system, I used the TRADES code, that performs the T_0s fitting during the numerical orbital integration.

3.1 TTV ANALYSIS: NUMERICAL SIMULATIONS

I used the Python version of TRADES, that implements the emcee code (Foreman-Mackey et al., 2013), a Python package for Bayesian analysis. I initialized the TRADES input files, using *Kepler*-279 properties. I set the epoch of the elements at the *Kepler* starting date, and the time duration of the integration $t_{\rm int} = 1460$ days, spanning all the *Kepler* mission. TRADES needs the list of the observed T_0s with uncertainties of each transiting body, which I report in Table A1, A2, A3 in Appendix A.
As stellar parameters, I assumed $R_{\star \rm SB} = 1.52 \pm 0.13$, as determined in Section 2.2.3, and $M_\star = 1.10 \pm 0.16$, from the NASA Exoplanet Archive.
Concerning the planetary parameters ($M_{\rm p}$, $R_{\rm p}$, P, e, ω, $\mathcal{M}$, i, Ω), the code requires an initial guess value and a minimum and maximum value, delimiting the interval to search in: in that range, TRADES assumes flat-uninformative prior distributions for the Bayesian analysis. I calculated the initial mass value of *Kepler*-279b using the Weiss & Marcy (2014) mass-radius relation $M_{\rm p}/M_\oplus = 2.69(R_{\rm p}/R_\oplus)^{-0.93}$, since no values were present in literature; for *Kepler*-279c and *Kepler*-279d I adopted the only literature mass values (Xie, 2014). The mass range spaces from values corresponding to a Earth-like planet up to Jupiter-like planets. For the planetary radius radius, I assumed the $R_{\rm p,SB}$ values (see Table 8) as initial guess and a radius range including values from 0.01 $R_\oplus$ up to 1 R_J, taking a conservative approach. I used Morton et al. (2016) planetary periods and I chose a period interval ± 2 days around the initial value, big enough to include all the possible TTV variations, but small enough to avoid overlapping with other transits. Concerning all the other parameters, they were free to vary in the whole domain. For the initial guess values, I assumed almost-circular orbits ($e = 0.0001$), $\Omega = 180°$, because outside the Solar System the reference system is arbitrary, and, since all the planets are transiting and no inclination measurements were present in literature, I assumed for the moment $i = 90°$ for each body.

In fact, as Borsato et al. (2014) tested on the *Kepler*-9 system, the assumption of coplanar orbits does not affect significantly the results of the simulation. I calculated $\mathcal{M}$ at the reference epoch t_0, $\mathcal{M}_0 = \frac{2\pi}{P}(t_0 - \tau)$, as

$$\mathcal{M}_0 = \mathcal{M}_{TT} + \Delta\mathcal{M} = \frac{2\pi}{P}(t_0 - t_{TT}), \tag{22}$$

where t_{TT} is the time of the first transit, $\Delta\mathcal{M} = \mathcal{M}_0 - \mathcal{M}_{TT}$, and $\mathcal{M}_{TT} = \frac{2\pi}{P}(t_{TT} - \tau)$ is the mean anomaly at the moment of the transit, with τ corresponding to the time of passage at the pericenter. The calculation is based on the assumption of a reference system defined such as $\omega = 90°$ and $\mathcal{M}_{TT} = 0$ at the moment of the transit. Table 9 lists the planetary parameters values adopted for the simulations.

I decided to fit M_p, P, e, $\mathcal{M}$, and ω: these physical parameters are derived from a computational convenient set of parameters, that TRADES actually fits, which are P, $\sqrt{e}\cos\omega$, $\sqrt{e}\sin\omega$, $M_p/M_\star$, and λ, where $\lambda = \omega + \Omega + \mathcal{M}$ is the mean longitude. I fixed the longitude of the node (for definition), the inclination, and the radius of each planet, because it is not possible to obtain with TRADES an estimate of R_p using only the T_0s and the TTV signal. I set the number of walkers (or chains) to use $n_w = 50$, and the number of runs for each walker $n_r = 50000$: each walker is a set of fitting parameters initialized close to the initial guess value with a Gaussian. I discarded the first 25000 steps as burn-in, and I used a thinning parameter $u = 100$, that is I kept only 1 step every 100 to reduce the autocorrelation of the steps.

I ran three different sets of simulations. In Simulation Set 1, I fitted M_p, P, e, $\mathcal{M}$, and ω for each planet, assuming an initial inclination $i = 90°$. In Simulation Set 2, I fixed M_b, keeping all the other parameters as in Simulation Set 1. Finally, in Simulation Set 3 I used the inclination value $i = 89.57$, derived from *Kepler*-279c transit fit. The third set is in turn divided into two further sets: the Simulation Set 3a, with no constraints on planetary eccentricities, and the Simulation Set 3b, with the constraint $e < 0.1$.

3.2 SIMULATION SET 1

I ran the Simulation Set 1 with the parameters specified in Section 3.1, fitting M_p, P, e, $\mathcal{M}$, and ω for each planet. I took as the best-fit parameter set the Maximum Likelihood Estimation (MLE) of the posterior distributions (within the High Density Interval, HDI), that is the set that maximizes the log-likelihood, defined as

$$\ln\mathcal{L} = -\ln(2\pi)\frac{dof}{2} - \frac{\sum\ln\sigma^2}{2} - \frac{\chi^2}{2}, \tag{23}$$

Table 9: Planetary parameters in TRADES input files.

***Kepler*-279b**

Parameter	Value	Min	Max
M_p [M_J]	0.028	0.003	1
R_p [R_J]	0.328	0.0008	1
P [days]	12.309	10.309	14.309
e	0.0001	0	1
ω [°]	90	0	360
$\mathcal{M}$ [°]	159.447	0	360
i [°]	90	0	180
Ω [°]	180	0	360

***Kepler*-279c**

Parameter	Value	Min	Max
M_p [M_J]	0.155	0.003	1
R_p [R_J]	0.500	0.0008	1
P [days]	35.735	33.735	37.735
e	0.0001	0	1
ω [°]	90	0	360
$\mathcal{M}$ [°]	156.494	0	360
i [°]	90	0	180
Ω [°]	180	0	360

***Kepler*-279d**

Parameter	Value	Min	Max
M_p [M_J]	0.118	0.003	1
R_p [R_J]	0.425	0.0008	1
P [days]	54.420	52.420	56.420
e	0.0001	0	1
ω [°]	90	0	360
$\mathcal{M}$ [°]	240.558	0	360
i [°]	90	0	180
Ω [°]	180	0	360

where dof= degrees of freedom. I computed the set of corresponding physical parameters, listed in Table 10: from now on, in each simulation set, I will refer to the values obtained in this way as the representative solution for the orbital parameters of the planets.
The $O-C$ diagrams with TRADES fit and residuals are shown in Figure 23, and the outcome of the fit is $\chi^2_r = 7.75$. In order to compare the goodness of two or more fits with different number of dof, the Bayesian Information Criterion (BIC=$\chi^2 + n_{\rm fit}\log(N)$, where $n_{\rm fit}$ is the number of fitted parameters and N is the number of the data) is needed. For the Simulation Set 1, I obtained BIC=1263.60.

As Table 10 shows, *Kepler*-279b mass is almost unconstrained and only an upper limit can be determined. This is probably due to the fact that TRADES interprets the TTV signal of planet b as scatter or noise: in fact, the $O-C$ fit reproduces a linear trend without sinusoidal modulations (Fig. 23).

Table 10: Derived parameters of the *Kepler*-279 system from the Simulation Set 1.

Parameter	*Kepler*-279b	*Kepler*-279c	*Kepler*-279d
M_p [$M_\oplus$]	$41.91^{+16.44}_{-41.53}$	$8.30^{+3.32}_{-2.46}$	$4.61^{+1.93}_{-1.28}$
P [day]	$12.31007^{+0.00009}_{-0.00013}$	$35.75944^{+0.01436}_{-0.02688}$	$54.45272^{+0.01136}_{-0.02620}$
e	$0.144^{+0.017}_{-0.139}$	$0.037^{+0.013}_{-0.026}$	$0.089^{+0.007}_{-0.034}$
$\mathcal{M}$ [°]	$168.40^{+125.28}_{-12.08}$	$147.59^{+11.34}_{-10.75}$	$262.92^{+5.62}_{-7.50}$
ω [°]	$80.2^{+14.5}_{-12.28}$	$99.7^{+11.0}_{-11.7}$	$63.2^{+9.5}_{-5.6}$

Moreover, *Kepler*-279c and *Kepler*-279d have low mass values, considering the input radii: they are located in the low-density region of the mass-radius diagram, as Figure 24 shows ($\rho_{\rm c} = 347.7 \pm 183.0$ kg/m^3, $\rho_{\rm d} = 269.0 \pm 139.0$ kg/m^3). Even though they are consistent with the composition of the so-called "mini-Jupiter" (such as *Kepler*-11e, or the *Kepler*-51 system), their peculiar densities required a deeper analysis.

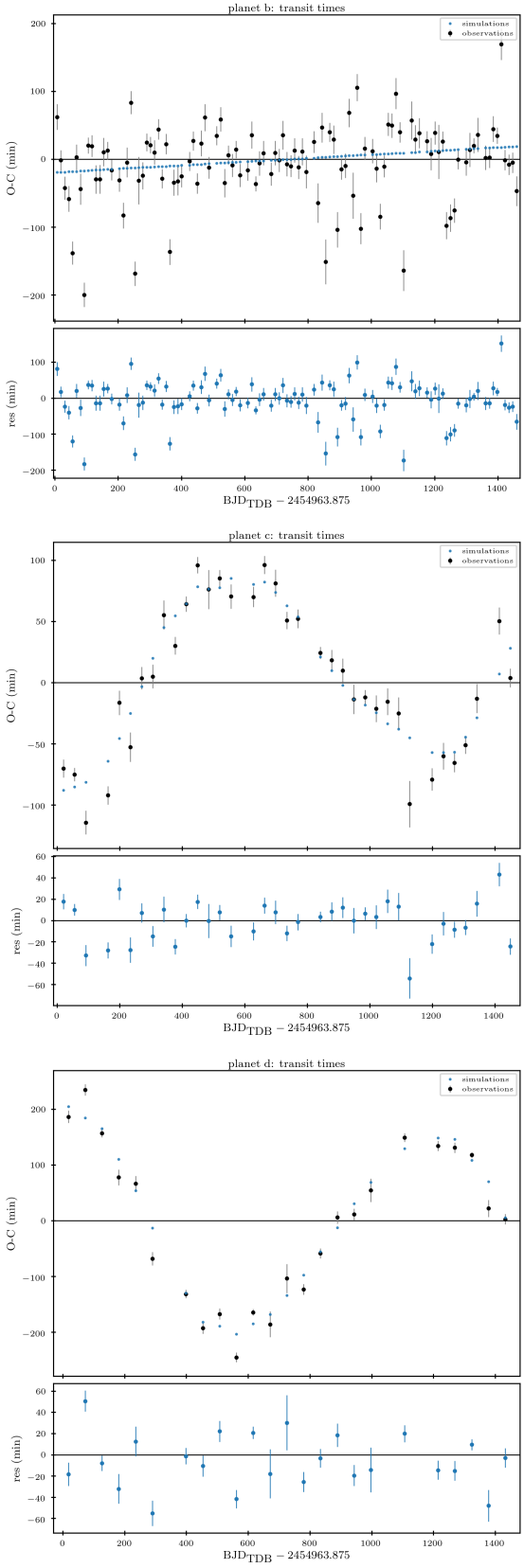

Figure 23: $O - C$ diagrams, with residuals, of *Kepler*-279b (top left panel), *Kepler*-279c (top right panel), and *Kepler*-279d (bottom panel) from the Simulation Set 1: observations are plotted as black circles, simulations are plotted as blue circles.

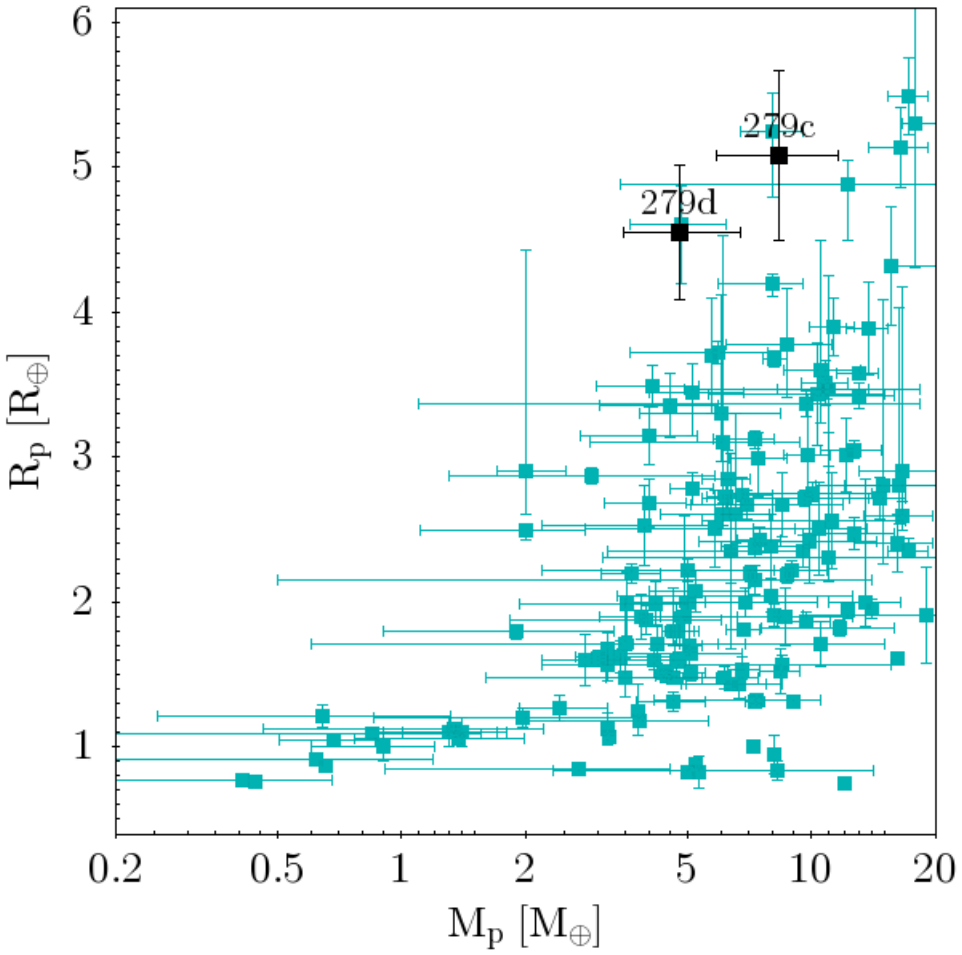

Figure 24: Mass-radius diagram for transiting exoplanets with known mass, based on the NASA Exoplanet Archive as August 2018; the x-axis is in logarithmic scale. *Kepler*-279c and *Kepler*-279d, with mass values from the Simulation Set 1, are highlighted with black squares.

3.3 SIMULATION SET 2

In order to improve the $O-C$ fit and the mass estimation of planets c and d, in the Simulation Set 2 I fixed *Kepler*-279b mass at $M_b = 9.036 \pm 2.37\, M_\oplus$, value obtained from the Weiss & Marcy (2014) mass-radius relation. The physical parameters derived from the MLE posterior distributions are listed in Table 11. The $O-C$ fit (Fig. 25) has $\chi^2_r = 7.79$ and BIC=1270.95, a slightly higher value than the one obtained in the Simulation Set 1.
The comparison among Table 10 and Table 11 shows that the derived M_p did not change significantly from the Simulation Set 1, and consequently the densities neither.

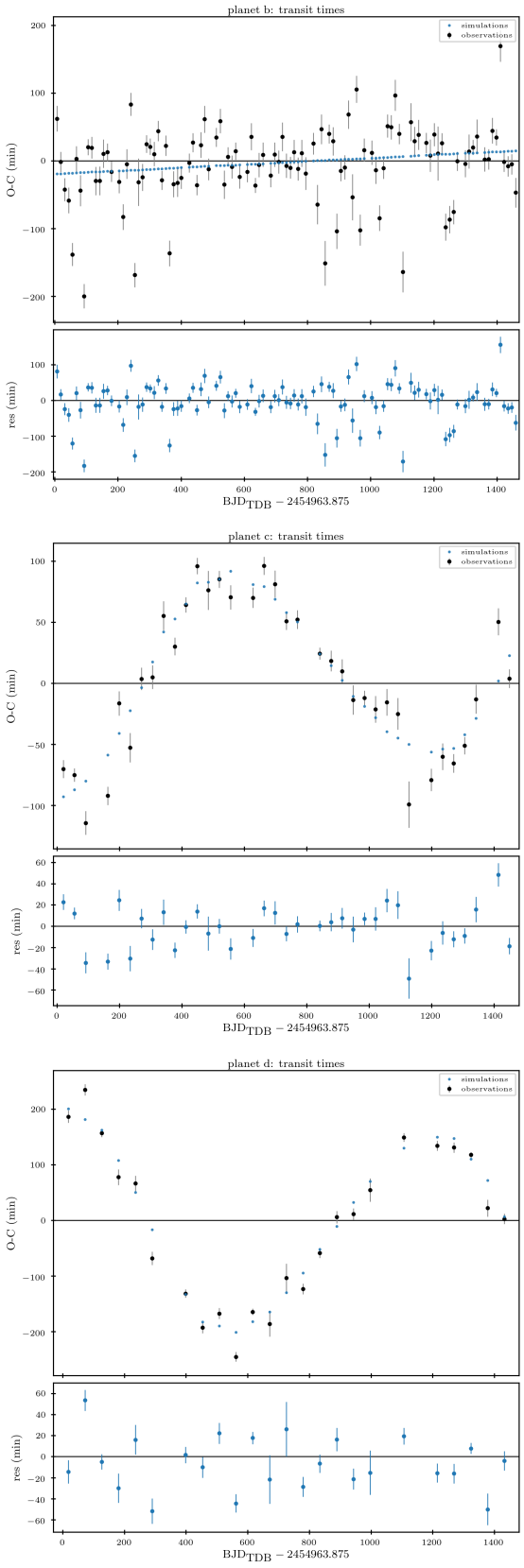

Figure 25: Same as Fig. 23, but for Simulation Set 2.

Table 11: Derived parameters of the *Kepler*-279 system from the Simulation Set 2.

Parameter	*Kepler*-279b	*Kepler*-279c	*Kepler*-279d
M_p [$M_\oplus$]	9.036 (fixed)	$7.58^{+3.46}_{-1.28}$	$4.33^{+1.55}_{-0.82}$
P [day]	$12.30995^{+0.00010}_{-0.00005}$	$35.73822^{+0.00065}_{-0.00006}$	$54.44336^{+0.00055}_{-0.00256}$
e	$0.099^{+0.007}_{-0.084}$	$0.008^{+0.004}_{-0.008}$	$0.075^{+0.003}_{-0.019}$
$\mathcal{M}$ [°]	$120.02^{+77.97}_{-10.21}$	$141.01^{+218.99}_{-141.00}$	$-86.17^{+5.84}_{-3.40}$
ω [°]	$128.8^{+16.9}_{-96.92}$	$105.8^{+162.99}_{-55.7}$	$51.5^{+3.7}_{-5.6}$

3.4 SIMULATION SET 3

In the Simulation Set 1 and 2, I assumed coplanar orbits with $i = 90°$. In the Simulation Set 3, I decided to investigate the effect of a different input inclination on the derived parameters.

I decided to model the transit of *Kepler*-279c, because its orbital period corresponds to the first main peak identified in the BLS periodogram, so the transit has the highest SNR. First, I considered for each transit the time region $\Delta T = T_0 \pm 0.5$ days, containing the whole transit and a portion of the stellar continuum, and I removed the data points (24%) with a SAP Quality Flag[1] $\neq 0$. Inside that interval, I selected the out-of-transit region as the external range of $T_0 \pm T_{\rm dur}$, where $T_{\rm dur}$ is the duration of the transit (Table 3), and I performed a linear fit[2], which I removed from the light curve around the transit. Finally, I performed the phase-folding of the detrended light curve at *Kepler*-279c period $P_{\rm c}$, such that T_0 corresponded to $\phi = 0.5$: because of the code implementation, I re-converted the phase in physical units (days) multiplying for $P_{\rm c}$.
I analyzed the detrended-folded SLC with a Python code (courtesy of Borsato et al., in prep.), that uses the `emcee` module and models the transit with the `batman` package (Kreidberg, 2015). The code allows the fitting of $\log_{10}(\rho_\star)$, with $\rho_\star$ the stellar density, $\sqrt{k}$, $\sqrt{b}$, with b the impact parameter, T_0, a quadratic limb darkening law with q_1 and q_2 terms Kipping (2014), and the jitter parameter in the form of $\log_2(\sigma_{\rm j})$. All the parameters have physical and meaningful boundaries with uniform-uninformative priors, but the $\log_{10}(\rho_\star)$, which prior has been computed from the values and uncertainties of $M_\star$ and $R_{\star,\rm SB}$ (determined in Section 2.2.3). I initialized

[1] The SAP Quality flag indicates when certain spacecraft events occurred or when the pipeline flagged interesting phenomenon, like rolling band artifacts or cosmic rays occurrence. For the summary of the flags, see the *Kepler Archive Manual*.
[2] For the linear fit, I used the Python `scipy.odr` package.

50 walkers with a hyper-Gaussian based on the values from the previous analysis and literature (Morton et al., 2016), then I ran the analysis for 100000 steps, discarding the first 50000 steps as burn-in, and I applied a thinning factor of 100. I took as the best-fit parameter set the MLE (see Fig. 26 for the fitting model and residuals) of the posterior distributions (within the HDI), and I computed the derived (physical) parameters.

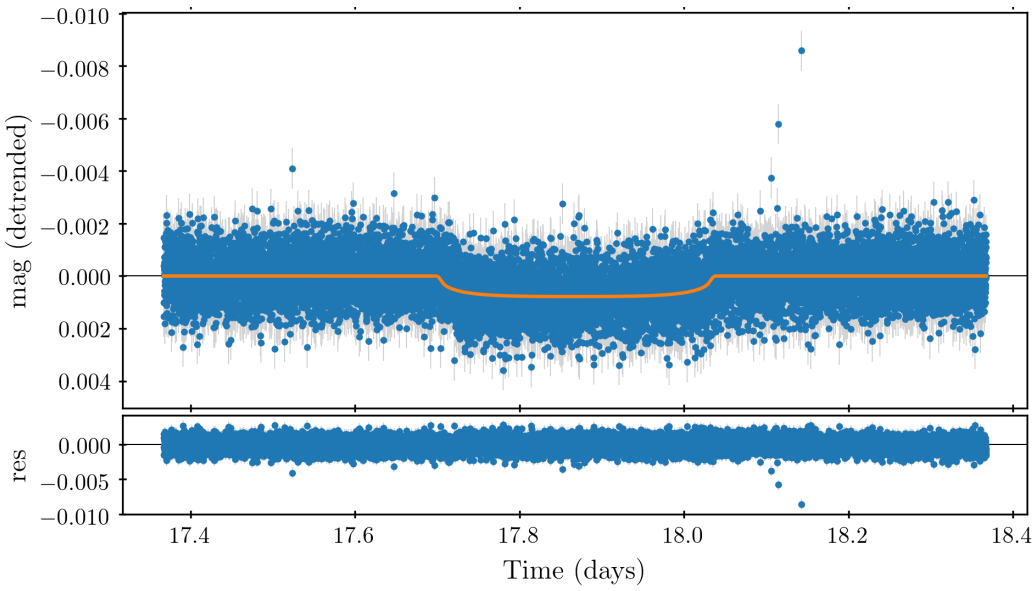

Figure 26: Detrended and folded SCL (blue circles), showing the fit of *Kepler*-279c transit (orange line) obtained from the `emcee` analysis.

As this transit fit was not the initial purpose of this work, I will only report the two parameters that are more meaningful for the next analysis, the planetary radius and the inclination of the orbit. I computed R_c from the $\sqrt{k}$ using $R_{\star,\mathrm{SB}}$, and I found $R_{c,\mathrm{fit}} = 4.04^{+0.48}_{-0.35}\,R_\oplus$, that is lower but consistent with $R_{p,\,\mathrm{SB}}$; I computed, from $\sqrt{b}$, an inclination $i = 89.57^{+0.42}_{-0.22}$, that I adopted in the next dynamical simulations.

3.4.1 Simulation Set 3a

I ran the Simulation Set 3a using the new inclination value, with the parameters specified in Section 3.1, and I fitted P, e, $\mathcal{M}$, and ω for each planet, and M_p for *Kepler*-279c and *Kepler*-279d. As in the Simulation Set 2, I decided to fix M_b, because *Kepler*-279b $O-C$ diagram does not show sinusoidal modulations, and `TRADES` can only reproduce a linear trend. Moreover, the TTV signals of *Kepler*-279c and *Kepler*-279d do not show any signature related to the presence of *Kepler*-279b and its gravitational interaction. Under these conditions, no information on M_b can be extracted through a TTV analysis.

The derived parameters computed from the MLE solution are listed in Table 12.

Table 12: Determined parameters of the *Kepler*-279 system from the Simulation Set 3a.

Parameter	*Kepler*-279b	*Kepler*-279c	*Kepler*-279d
M_p [$M_\oplus$]	9.036 (fixed)	$14.49^{+1.82}_{-5.55}$	$8.07^{+1.81}_{-3.14}$
P [day]	$12.30963^{+0.00061}_{-0.00009}$	$35.73792^{+0.00048}_{+0.00247}$	$54.43353^{+0.00158}_{-0.00107}$
e	$0.103^{+0.034}_{-0.014}$	$0.319^{+0.023}_{-0.045}$	$0.310^{+0.015}_{-0.040}$
$\mathcal{M}$ [°]	$176.71^{+4.79}_{-20.43}$	$171.99^{+1.77}_{-17.40}$	$257.35^{+1.94}_{-14.07}$
ω [°]	$70.7^{+26.6}_{-7.7}$	$59.3^{+35.2}_{-3.8}$	$57.1^{+29.2}_{-3.2}$

Figure 27, 28 show the correlation plot for the fitted and derived posterior distributions, respectively. The $O-C$ diagrams are shown in Figure 29, and the outcome of the MLE fit is $\chi^2_r = 7.63$ (BIC=1248.67): since the BIC is lower than the previous ones, for the moment I assumed the Simulation Set 3a solution as the best one.
The obtained mass values are higher than the previous simulations ones, and so the densities, $\rho_c = 606.9 \pm 311.8$ kg/m^3 and $\rho_d = 470.8 \pm 232.3$ kg/m^3. *Kepler*-279c has an even higher density ($\rho_c = 1207.9 \pm 632.0$ kg/m^3), if the radius $R_{c,fit}$ (see Sec. 3.4) is assumed[3]. Assuming these parameters, the planets are located in a more populated region of the mass-radius diagram (see Figure 30).

The eccentricities of the three planets are atypically high, while the analysis of multiple planetary systems usually show circular orbits (Hadden & Lithwick, 2014; Van Eylen et al., 2018), due to the damping mechanisms related to planetary interactions.
In the correlation plot, some accumulation zones of the solutions are stressed at low eccentricity. I decided to investigate the low-e region of the posterior parameters distribution, in order to possibly highlight a different set of solutions.

[3] As the radius determination was not the initial purpose of this work, I did not calculate *Kepler*-279d radius through the transit fit.

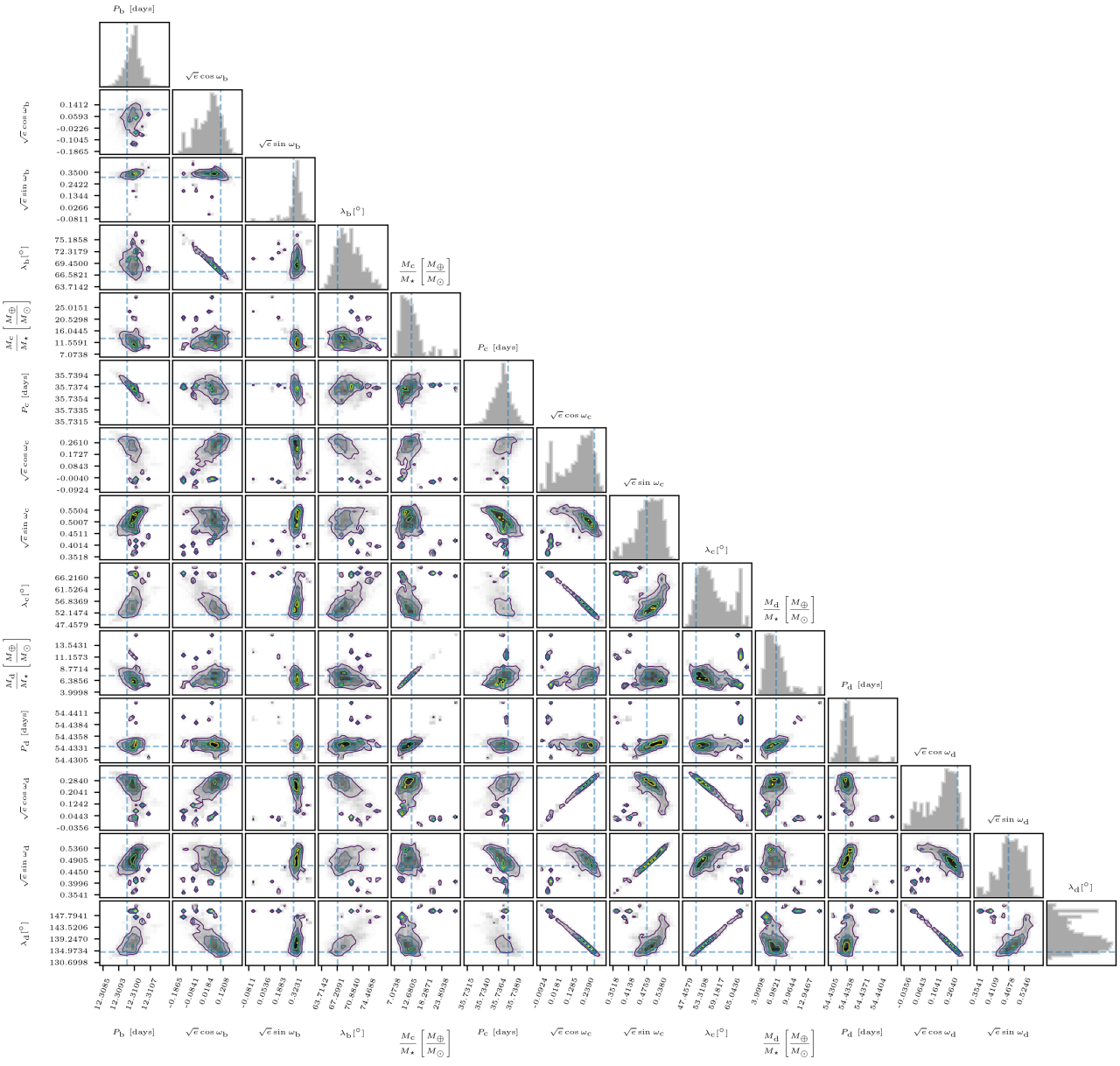

Figure 27: MLE posterior distributions of the Simulation Set 3a.

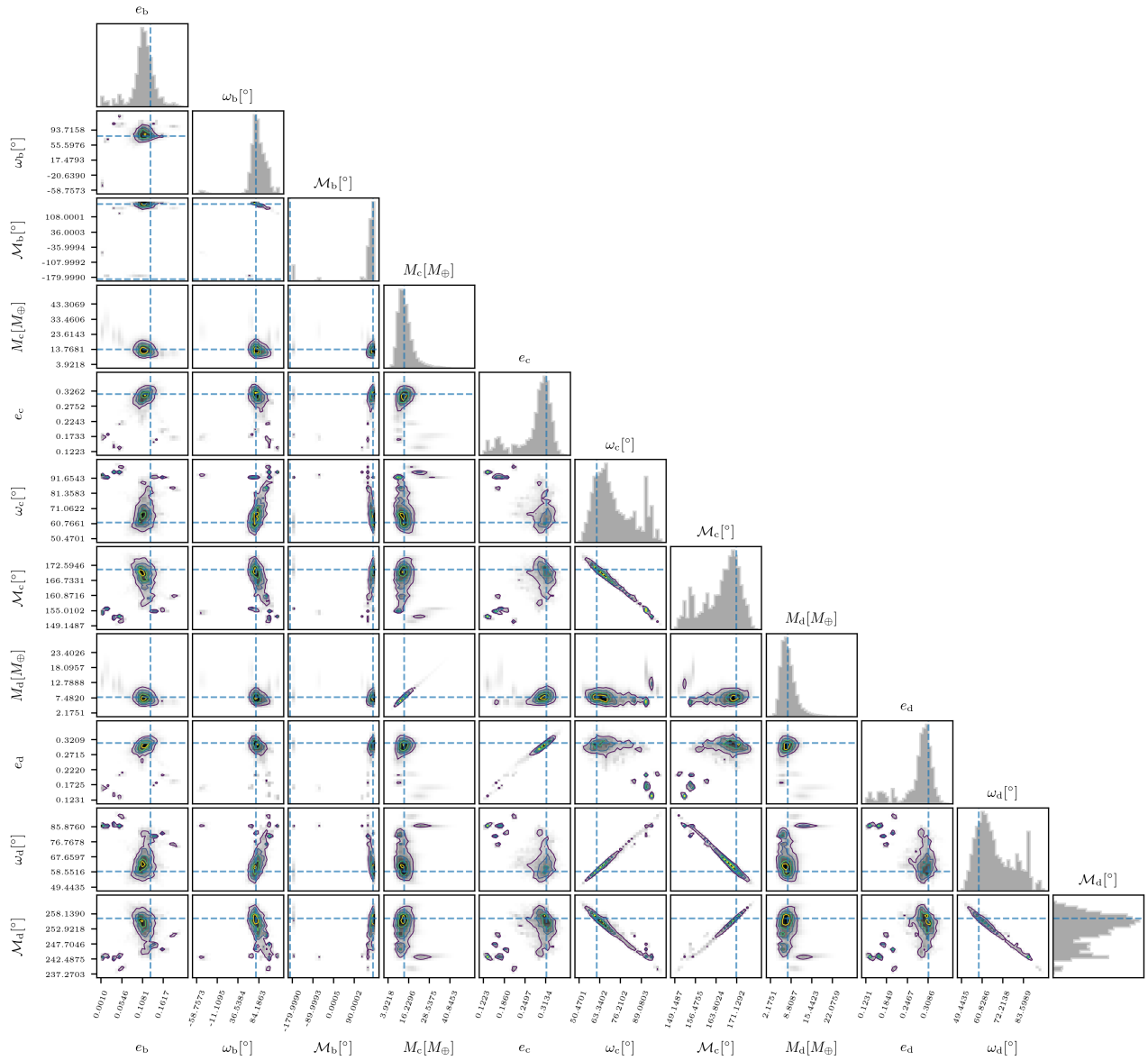

Figure 28: Derived posterior distributions of the physical parameters computed from the MLE of the Simulation Set 3a.

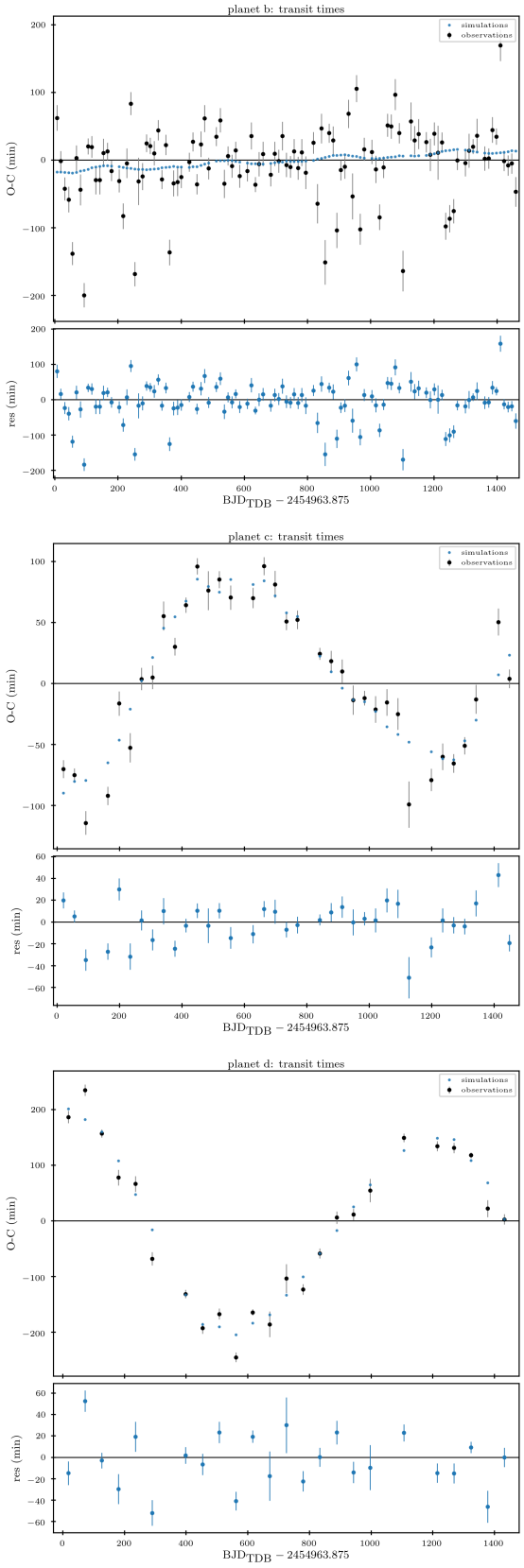

Figure 29: Same as Fig. 23, but for the Simulation Set 3a.

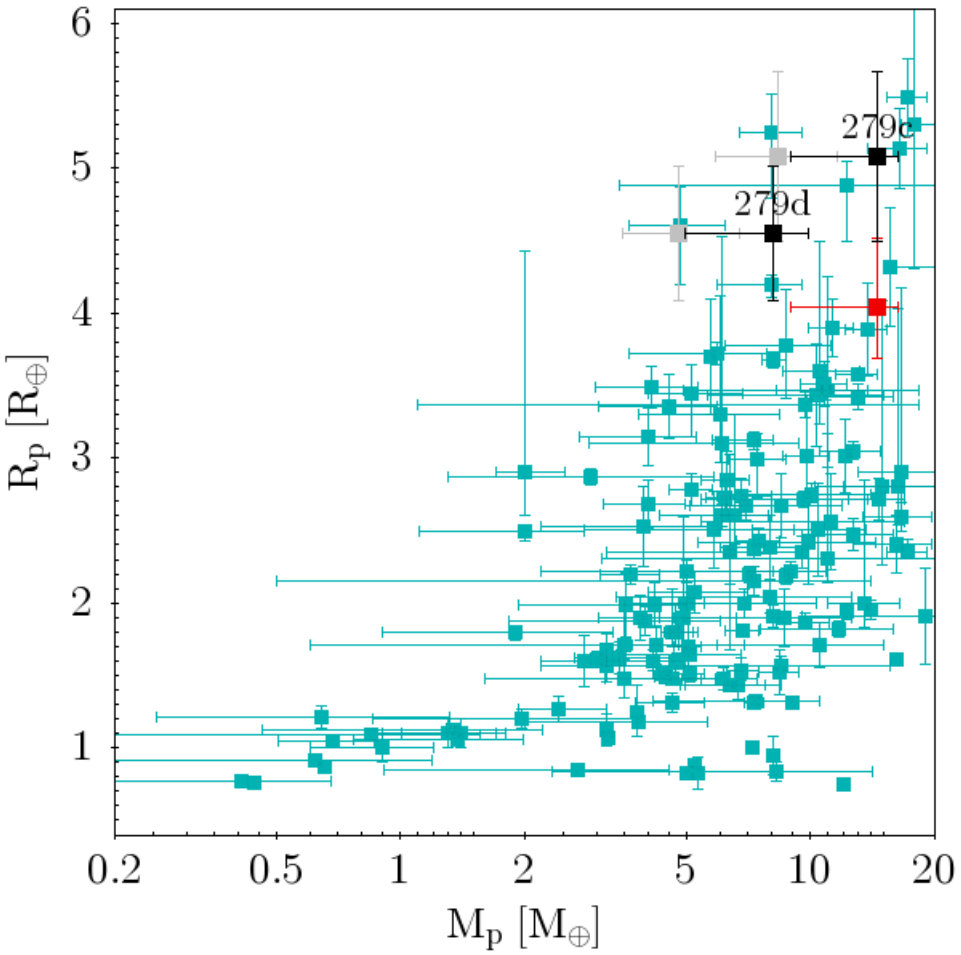

Figure 30: Mass-radius diagram for transiting exoplanets with known mass, based on the NASA Exoplanet Archive as August 2018. *Kepler*-279c and *Kepler*-279d, with mass values from the Simulation Set 3a, are highlighted with black squares. The gray squares show, for comparison, the position of the planets with M_c, M_d from the Simulation Set 1. The red square indicates *Kepler*-279c position with M_c from Simulation Set 3a and radius calculated from the transit fit: the two R_c values agree within the errorbars.

3.4.2 Simulation Set 3b

I ran the Simulation Set 3b constraining the eccentricity $e < 0.1$ and fitting the same parameters of the Simulation Set 3a. The derived parameters computed from the MLE solution are listed in Table 13, and Figure 31, 32 show the correlation plot for the fitted and derived posterior distributions, respectively. The $O - C$ fit of the MLE solution is almost equal to the previous one (Fig. 33), yielding to $\chi^2_r = 7.77$ (BIC=1270.48), that is slightly higher than the high-e solution. Note that the planetary masses are considerable lower, implying the location of planets c,d in the low-density, less populated region of the mass-radius diagram.

Table 13: Determined parameters of the *Kepler*-279 system from the Simulation Set 3b.

Parameter	*Kepler*-279b	*Kepler*-279c	*Kepler*-279d
M_p [$M_\oplus$]	9.036 (fixed)	$7.70^{+2.97}_{-2.20}$	$4.23^{+1.90}_{-0.88}$
P [day]	$12.31006^{+0.00046}_{-0.00004}$	$35.73889^{+0.00041}_{-0.00039}$	$54.43104^{+0.00202}_{-0.00079}$
e	$0.065^{+0.027}_{-0.034}$	$0.083^{+0.017}_{-0.012}$	$0.025^{+0.026}_{-0.005}$
$\mathcal{M}$ [°]	$270.57^{+55.14}_{-2.00}$	$1.16^{+3.40}_{-20.81}$	$-9.63^{+57.32}_{-8.84}$
ω [°]	$333.7^{+0.5}_{-49.6}$	$249.1^{+18.0}_{-2.3}$	$337.4^{+8.6}_{-55.8}$

Since the dynamical analysis had highlighted the presence of two families of solutions, one with high-e values and one with low-e values with very close χ^2_r, I checked in Chapter 4 the stability of the system in both cases, in order to determine a unique solution for the orbital parameters of the planets.

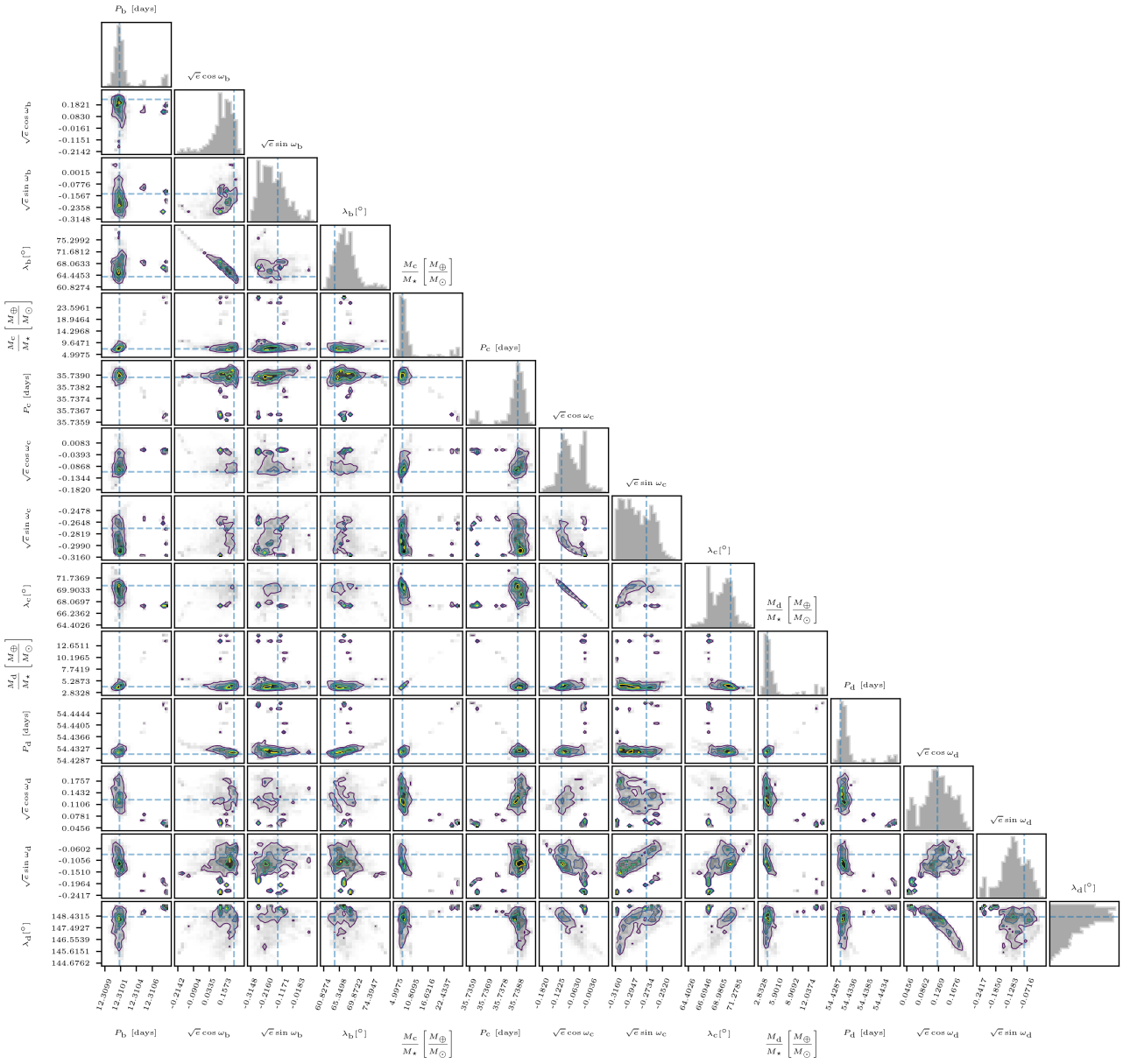

Figure 31: MLE posterior distributions of the Simulation Set 3b.

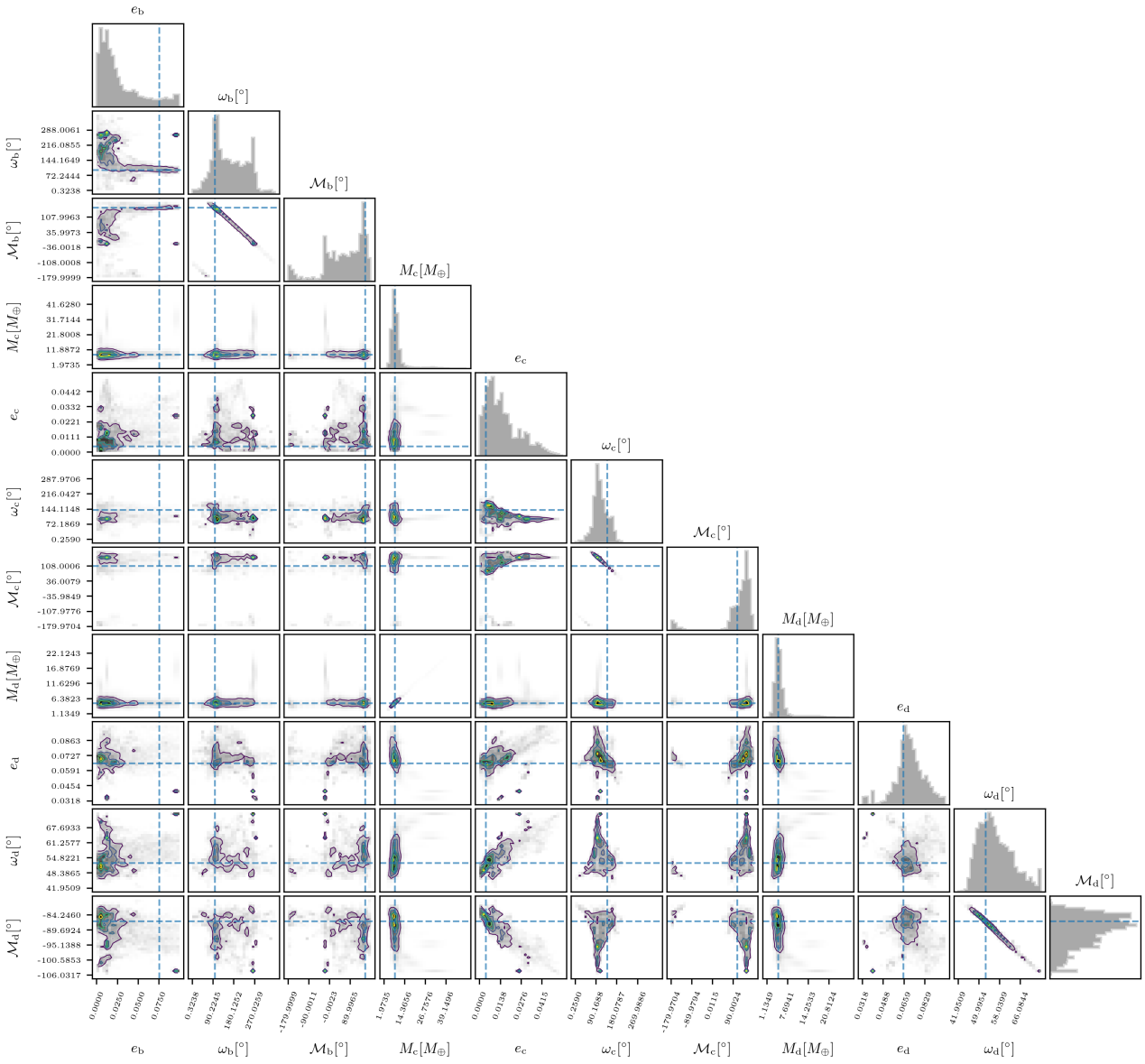

Figure 32: Derived posterior distributions of the physical parameters computed from the MLE of the Simulation Set 3b.

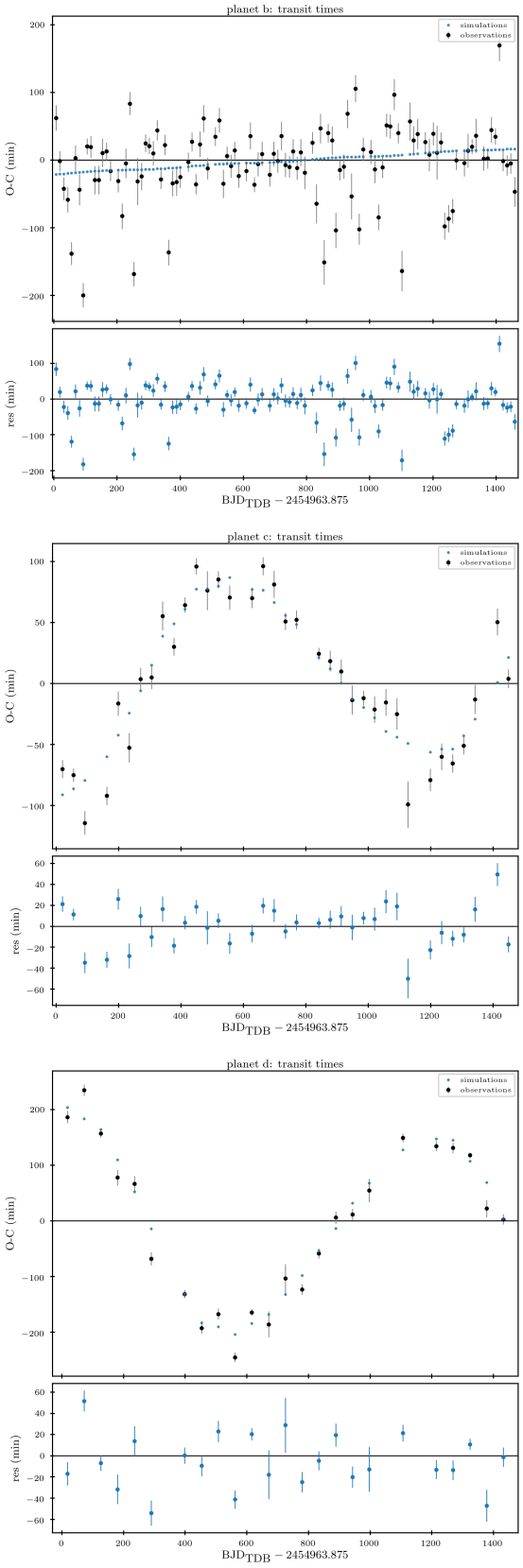

Figure 33: Same as Fig. 23, but for the Simulation Set 3b.

4 STABILITY ANALYSIS

4.1 STABILITY WITH THE FREQUENCY MAP ANALYSIS

I used the output parameters of the `TRADES+emcee` simulations to perform an N-body integration with `SyMBA` (Symplectic Massive Body Algorithm), a time-reversible symplectic algorithm (Duncan et al., 1998), and I checked the stability of the results with the Frequency Map Analysis tool (FMA; Laskar et al. 1992; Laskar 1993a,b). The FMA technique is used for determining the frequency vector of a dynamic system: the method is based on the analysis of the evolution with time of the fundamental frequencies that appear in the spectrum of a body orbital elements, and the amount of diffusion of the frequencies gives a measure for the stability of an orbit (Marzari et al., 2002). Without entering in the mathematical and computational formalism (see the dedicated series of papers – Laskar et al. 1992; Laskar 1993a,b, 1999), I report a qualitative description of the algorithm used to perform the stability analysis with the FMA technique, which details are reported in Marzari et al. (2002).

Using the orbital parameters determined from the numerical integration of the orbits with `SyMBA`, the algorithm calculates the frequencies of the circulation of the pericenter longitude[1] $\tilde{\omega}$, applying the Fourier transform over a running window spanning the total integration time, for a total of 10 overlapping windows. The proper frequency g is computed on each running window, and the standard deviation σ_g of the g-values over the total integration timespan is derived as a measure for the diffusion rate of the orbit. Following the prescriptions of Marzari et al. (2002), a system is considered stable if the diffusion coefficient $\epsilon = -\log(\sigma_g/g)$ is > 4, in an unstable or chaotic state otherwise. This can be understood qualitatively considering that, if the orbit is chaotic, the value of g in each temporal window would vary significantly and consequently the standard deviation would increase, yielding high values of σ_g/g, and so low values of ϵ. On the other side, if the orbit is regular all the values of g would almost coincide, yielding low values of σ_g, and consequently high ϵ values.

[1] The longitude of the pericenter is defined as $\tilde{\omega} = \Omega + \omega$, and it appears as a fundamental variable in secular theories (Marzari et al., 2002).

4.2 HIGH ECCENTRICITY SOLUTIONS

I first considered the Simulation Set 3a, with fixed *Kepler*-279b mass and no constraints on eccentricity[2]. From the output files, I extracted, as a representative sample, the first 100 sets of parameters with the highest log-likelihood, and I computed the orbital parameters (M_p, and Keplerian elements) needed for the orbital integration with the `SyMBA` code. I integrated each solution with `SyMBA` for 10^5 years, with a temporal step corresponding to 1/20 of the inner planet period. Then, I applied the FMA[3] on the 100 solutions in order to determine the coefficients of diffusion ϵ. According to Marzari et al. (2002) prescriptions, 97% of the solutions resulted to be in a stable configuration, with $\epsilon > 4$ for each body. I built the diffusion portrait of the 100 solutions in the logarithmic plane $M_c - M_d$, using the diffusion coefficient ϵ_c of planet c as representative coefficient for the stability (Fig. 34). In fact, *Kepler*-279c interacts gravitationally with *Kepler*-279d, so it is reasonable to assume that their orbital parameters changes are related; moreover, it is close to planet b, and so it is supposed to be influenced more than planet d by *Kepler*-279b orbital parameters changes, making its diffusion coefficient the best choice. Figure 35 shows that the stable solutions are located in every mass range, and no significant trends are stressed.

Finally, it is worth to note that the best-fit orbital solution computed from the MLE of the Simulation Set 3a, that I chose as representative solution (Table 12), resulted to be stable.

4.3 LOW ECCENTRICITY SOLUTIONS

I considered the `TRADES+emcee` simulation with fixed Kepler-279b mass and eccentricity[4] $e < 0.1$. I applied the same analysis described in Section 4.2 to the first 100 solutions with the highest log-likelihood. In this case, only 44% of the solutions resulted to be in a stable configuration. It is important to distinguish the cases in which the instability of a solution is due to low values of ϵ and the cases in which it is due to mergers between planets, or ejection of one planet during the orbital integration. In fact, orbits with low eccentricities imply a longer period $P_{\tilde{\omega}}$ of the circulation of pericenter longitude, and it is possible that, if the integration timespan is shorter than $P_{\tilde{\omega}}$, the determination of g is not accurate, yielding low ϵ values: in this case,

[2] The input parameters are listed in Sec. 3.4.1

[3] Planets c and d have a period commensurability suggesting a first-order MMR, so the study of $\tilde{\omega}$ proper frequency is a reliable method for the stability analysis (Marzari et al., 2006). However, in presence of MMRs of order> 1, the FMA has to be applied carefully, and the study of the resonant angle is needed.

[4] The input parameters are listed in Sec. 3.4.2.

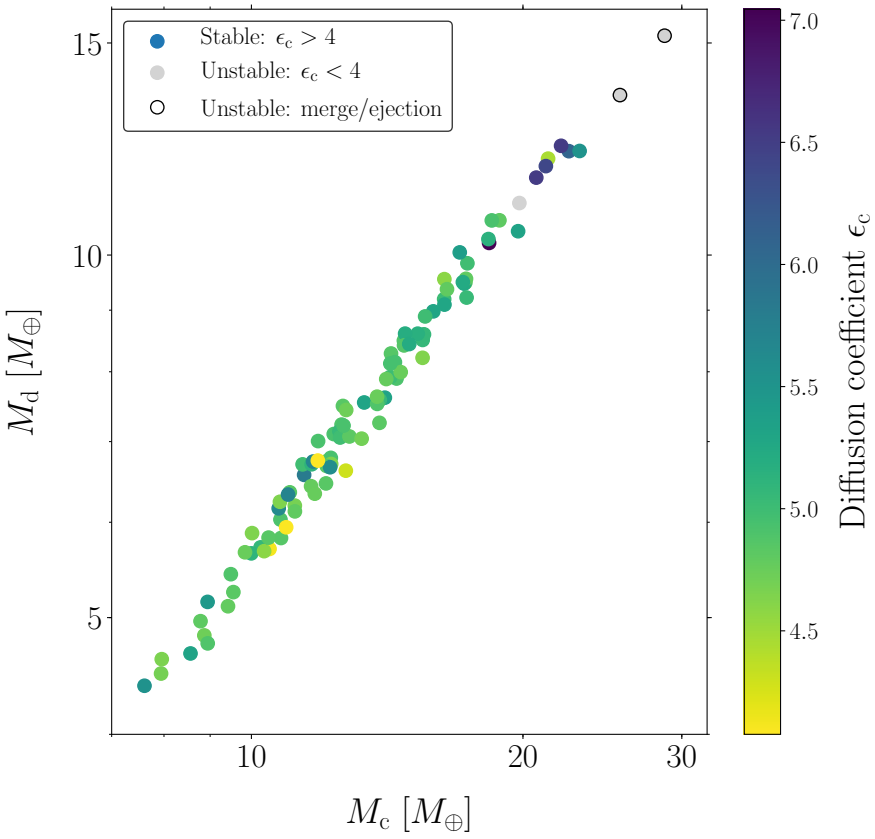

Figure 34: Stability plot of the 100 solutions at high-e with the highest log-likelihood; both axis are in logarithmic scale. The stable solutions are color-coded according to *Kepler*-279c diffusion coefficient $\epsilon_c = -\log(\sigma_g/g)$. The gray circles indicate the unstable solutions, both due to $\epsilon < 4$, or to mergers between planets or ejection of one planet during the orbital integration (black-encircled).

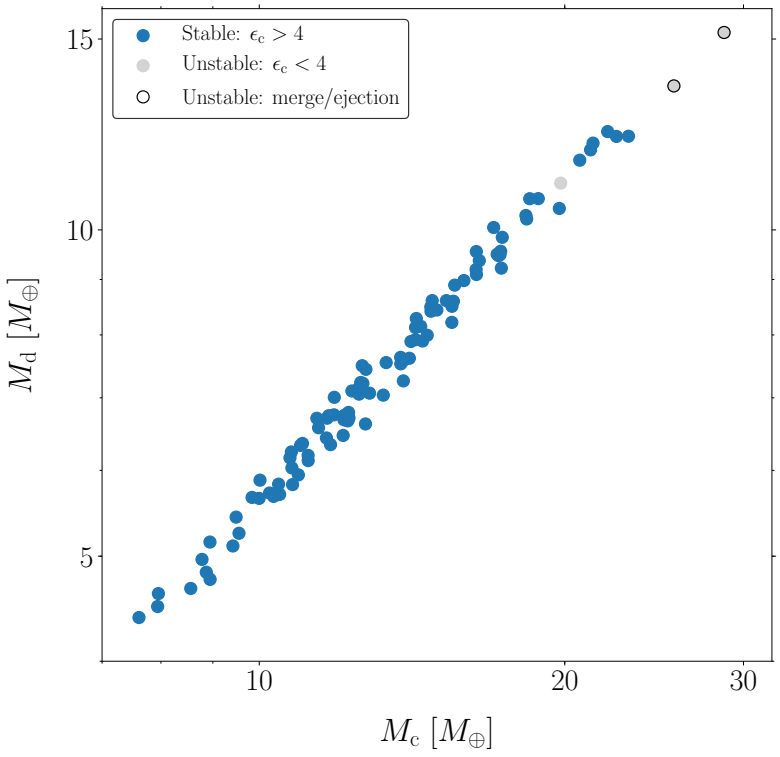

Figure 35: Same as Fig. 34, but showing all the stable solutions as blue circles, independently of their ϵ_c value, to stress the relative displacement of stable and unstable solutions.

a longer integration time is needed to compute the stability of the system in a proper way.
I checked the cause of the instability, and I found that 39 out of the 56 unstable solutions are due to mergers or ejections, while only 17 have diffusion coefficients > 4. Figure 36 shows the diffusion portrait of the 100 low-e solutions. As in the high-e case, no clear trends are stressed,

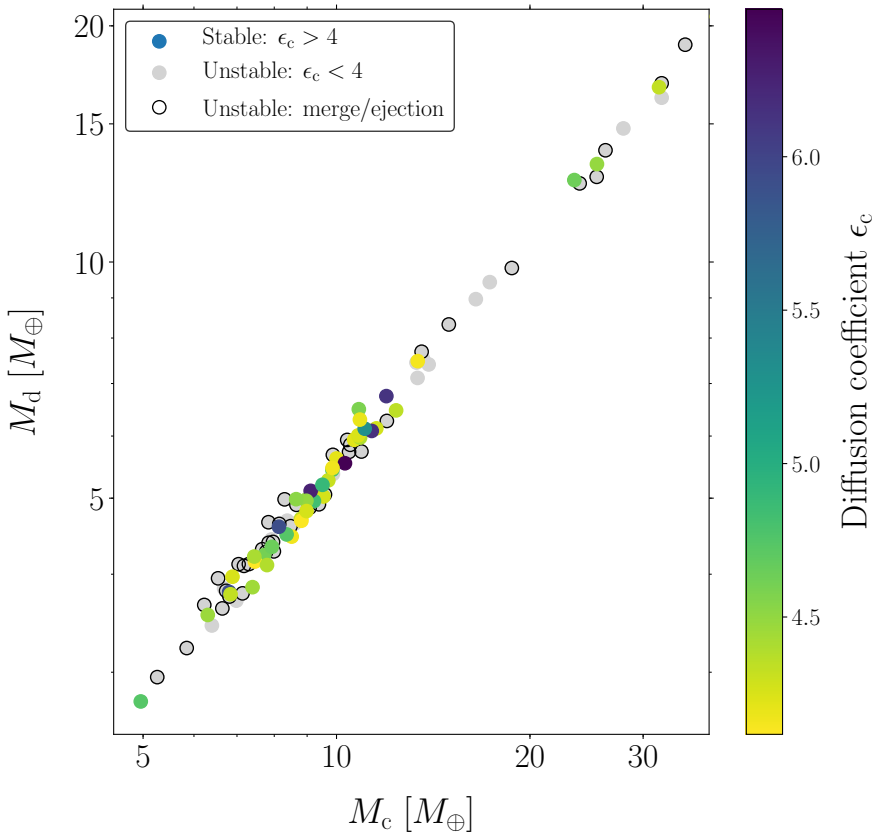

Figure 36: Same as Fig. 34, but for the 100 low-e solutions.

and both the stable and unstable solutions are locate almost uniformly in the plot (Fig. 37). Finally, differently from the high-e case, the best-fit orbital solution computed from the MLE of the Simulation Set 3b (Table 13) resulted unstable, due to a merger between planet c and d during the orbital integration. Considering that, in the high-e case, only two solutions out of 100 underwent mergers or ejections and only one had $\epsilon > 4$, I found that low-e solutions are generally affected by instability more than the high-e ones.

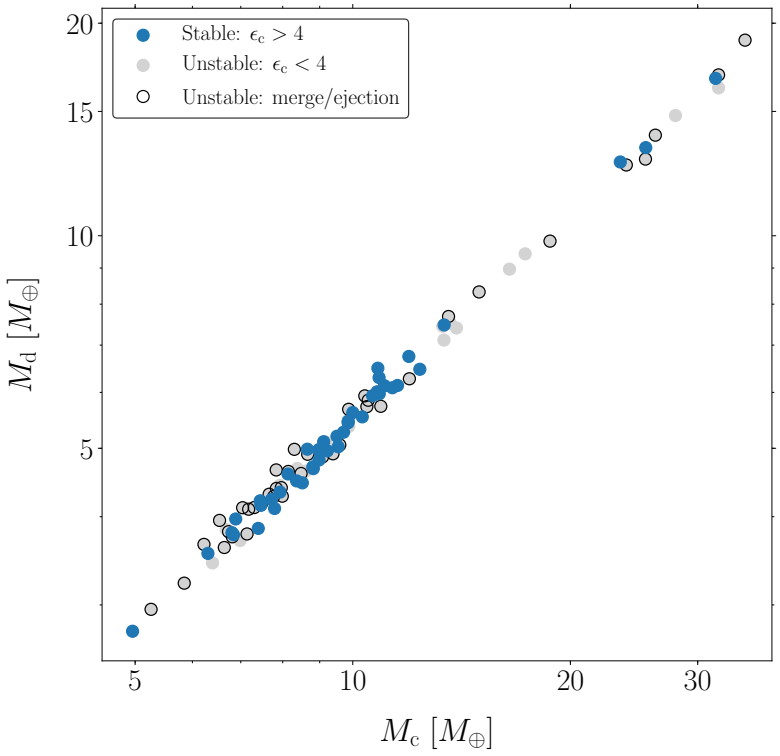

Figure 37: Same as Fig. 35, but for the 100 low-eccentricity solutions.

In the view of the stability analysis, I decided to adopt as unique solution the set of orbital parameters computed from the MLE in the Simulation Set 3a, with high-e values (Table 12). In fact, its log-likelihood and χ^2_r are higher than the low-e representative solution and, moreover, the solution is stable, as almost all of the high-e analyzed solutions. On the other side, more than half of the low-e analyzed solutions are chaotic or underwent mergers or ejections, and consequently it is unlikely that these orbital configurations could have survived for a timescale comparable with the stellar age.

SUMMARY AND CONCLUSIONS

The purpose of this thesis is to perform a dynamical study on a multiple planetary system, in order to determine the planetary parameters, and in particular M_p, through a TTV analysis. The planetary mass is essential for an exoplanet characterization: once R_p and M_p are known, the average density of the body can be obtained, allowing a first estimate of the inner bulk composition. Moreover, the improving of the mass-radius relation, the study of the internal composition, the computing of the dynamics of the systems and the understanding of the processes of formation and evolution are all related to the study of mass and density.

In my work, I decided to analyze the *Kepler*-279 system (KOI-1236), selected from the Holczer et al. (2016) catalog of *Kepler* planets showing a strong TTV signal. *Kepler*-279 is a main sequence F-type star ($T_{\rm eff} = 6366 \pm 259$ K, $M_\star = 1.10 \pm 0.16\, M_\odot$,$R_\star = 1.52 \pm 0.13 R_\odot$): I calculated $R_\star$ exploiting the new G-DR2 data, and the obtained value is in agreement with the literature ones (Rowe et al., 2014; Morton et al., 2016). *Kepler*-279 hosts three confirmed transiting planets ($R_b = 3.51 \pm 0.79\, R_\oplus$, $R_c = 5.08 \pm 0.58\, R_\oplus$, $R_d = 4.55 \pm 0.46\, R_\oplus$) and one planetary candidate, KOI-1236.04 ($R_{\rm KOI} = 4.13 \pm 0.92\, R_\oplus$). In order to confirm or reject the hypothesis of a fourth planet, I applied iteratively the BLS algorithm on the phase folded LLC, in order to individuate the transit signal corresponding to KOI-1236.04. The algorithm computes the periodogram of the LLC and it returns period, duration and depth of the main peak; then, it subtracts the corresponding transit model from the light curve before repeating the BLS search. I found no statistically significant signals corresponding to KOI-1236.04 period, so I classified the candidate as a False Alarm. As regards the three confirmed planets, *Kepler*-279c and *Kepler*-279d show a strong, anti-correlated TTV signal, that could be explained considering that the periods commesurability suggests a, or close to, 3:2 MMR: first-order MMRs produce the strongest TTV signals (Agol & Fabrycky, 2017). I exploited the TTV signal to perform three sets of numerical simulations with TRADES, a Python code (originally implemented in Fortran 90) that performs the T_0s fitting during the numerical orbital integration. In the Simulation Set 1, I fitted M_p, P, e, $\mathcal{M}$, and ω for each planet, assuming coplanar orbits with $i = 90°$: I obtained, as best-fit solution, $M_b < 43.56\, M_\oplus$, $M_c = 8.30^{+3.32}_{-2.46}\, M_\oplus$, and $M_d = 4.61^{+1.93}_{-1.28}\, M_\oplus$. Only an upper limit on M_b could be determined: *Kepler*-279b does not show a strong TTV signal, and no sinusoidal patterns were identified in its $O - C$ diagram (`TRADES` fit

reproduced a linear trend). In addition, M_c and M_d are low considering the input radii: even if they are consistent with the composition of very inflated "mini-Neptunes" (such as *Kepler*-11), the two planets are located in the low-density, less-populated region of the mass-radius diagram. In order to obtain a refined estimate of M_c and M_d, in the Simulation Set 2 I fixed $M_b = 9.036 \pm 2.37\, M_\oplus$, value obtained from the Weiss & Marcy (2014) mass-radius relation; however, the masses did not change significantly ($M_c = 7.58^{+3.46}_{-1.28}\, M_\oplus$, $M_d = 4.33^{+1.55}_{-0.82}\, M_\oplus$). In the Simulation Set 3, I investigated the effect of a different input inclination, $i = 89.57$, obtained from *Kepler*-279c transit fit. In this case, keeping M_b fixed, I obtained higher mass values, $M_c = 14.49^{+1.82}_{-5.55}\, M_\oplus$ and $M_d = 8.07^{+1.81}_{-3.14}\, M_\oplus$, that locate *Kepler*-279c and *Kepler*-279d in a more populated region of the mass-radius diagram. However, the eccentricites of the three planets were unexpectedly high ($e_b = 0.103^{+0.034}_{-0.014}$, $e_c = 0.319^{+0.023}_{-0.045}$, $e_d = 0.310^{+0.015}_{-0.040}$): compact, multiple systems usually require low e values in order to be stable (Hadden & Lithwick, 2014). Consequently, I investigated also the secondary, low-e region that is present in the correlation plot of the derived parameters: constraining $e < 0.1$, I obtained $M_c = 7.70^{+2.97}_{-2.20}\, M_\oplus$ and $M_d = 4.23^{+1.90}_{-0.88}\, M_\oplus$. In order to improve the T_0s determination's precision, and so the parameters estimate, a future perspective of this work is the re-calculation of all the planetary T_0s. After a suitable detrending of the original light curve (using the SAP flux, instead of the PDCSAP flux), an estimate of P can be obtained from the BLS analysis, and each transit can be fitted using the Bayesian approach described in Section 3.4. The procedure can be implemented in `TRADES`, modifying the code in order to perform the transit fit during the orbital integration: in this way, `TRADES` will become the first public photodynamical code.

The purpose of my work was the determination of a unique solution for the orbital parameters: since the high-e and low-e solutions had almost the same χ^2_r, I investigated the stability of the system in the two cases. I integrated with `SyMBA` the orbits of the 100 `TRADES` solutions with the highest log-likelihood for both the high and low eccentricity case, and I applied the FMA in order to obtain the diffusion coefficient ϵ, that give a measure of the stability of the orbits. I assumed the diffusion coefficient of *Kepler*-279c as representative for the stability of the system: according to Marzari et al. (2002) prescriptions, 97% of the high-e solutions were stable for the whole integration time ($t_{int} = 10^5$ yr), while only 44% of the low-e solutions resulted to be stable. The diffusion coefficient could be a non-reliable estimate for the stability if $t_{int} < P_{\tilde{\omega}}$, which is more probable in the low-e case. However, the majority (39) of the 56 unstable solutions shows instability due to mergers or ejections during the orbital integration, and this fact supports the hypothesis that, in my case, low-e solutions are intrinsically less stable than high-e ones.

In the view of the stability analysis, I adopted as final solution the set of orbital parameters with high-e determined in the Simulation Set 3: in fact, this solution is stable, while the low-e one resulted to be unstable. Moreover, the high-e solution has slightly lower $O-C$ residuals ($\chi^2_r = 7.63$) than the low-e one ($\chi^2_r = 7.77$).
Even if the majority of the observed multiple, compact systems shows low eccentricity values (Van Eylen et al., 2018), it is possible that, if planets c, d are effectively in a 3:2 MMR, the first-order resonance protects the system configuration, allowing the stability (at least for 10^5 yr) even at high eccentricities.

Since the stability analysis was not the main purpose of this work, I performed only a preliminar analysis: in the future, a deeper study will require the investigation of a more statistically robust sample of solutions with the FMA. In addition, especially in the low-e cases, the goodness of $\tilde{\omega}$ sampling while performing the FMA has to be checked: a suitable width of the temporal running window and a long enough integration time are needed for a solid result, and different combinations could be tested to find the optimal solution. Finally, the study of the resonant angle ψ is necessary to understand if planets c and d are effectively in a 3:2 MMR: if, rather than circulating, ψ is stationary, or librates (Perryman, 2014), then the planets are in resonance.

My final solution implies, in addition to *Kepler*-279b, the presence of two planets in resonance, with the inner one (*Kepler*-279c) more massive than the outer one (*Kepler*-279d). This configuration, instead of supporting a migratory history, suggests the so-called *inside-out* formation scenario: the inner planet forms earlier, and it induces the formation of the successive planet through the creation of a gravitationally unstable ring located in the resonant orbit, fed from a continuous stream of small ($\sim$ cm-m size) "pebbles", drifting inwards via gas drag (Chatterjee & Tan, 2014).

OUTLOOKS

In the next future, the NASA mission Transiting Exoplanet Survey Satellite (TESS) will provide a huge catalog of new transiting exoplanets: the analysis I performed on the *Kepler*-279 system could be applied on TESS exoplanets showing TTV signal. Moreover, TESS is observing bright stars to make easier the ground-base RV follow-up: if RV data are present, more precise orbital parameters can be determined with `TRADES`, which can fit at the same time RV and TTV data. In particular, a focus on the mass determination of Neptune-like or even smaller planets (R<5 $R_\oplus$) could provide insights into the atmospheres and gaseous envelopes formation processes. Moreover, interesting targets for the CHaracterising ExOPlanets Satellite (CHEOPS)

mission can be identified: CHEOPS, the first S-class mission from the European Space Agency (ESA) is going to improve the accuracy on radii measurements of Neptunian-like planets and Super-Earth. CHEOPS could also expand the baseline of observations for selected targets, allowing a more precise estimate of planetary parameters, in particular $M_{\rm p}$ (through TTV or RV analysis). Finally, a solid method for mass determination is essential for the ESA PLAnetary Transits and Oscillations of stars (PLATO) mission, that is going to detect terrestrial exoplanets in the habitable zone of solar-type stars. PLATO will allow us to measure how planet density and mass vary with orbital distance, planetary system architectures, and host star parameters (spectral type, composition, age), in order to gain new insights into planet formation and evolution processes. PLATO will also provide well-characterized targets for atmosphere spectroscopic studies, i.e. for the James Webb Space Telescope (JWST) or the European-Extremely Large Telescope (E-ELT). It will also provide accurate ages for a large sample of planetary systems, thanks to gyrochronology and asteroseismology. PLATO will transform our knowledge of habitable zone rocky planets and pave the way for the detection of life beyond the Solar System.

APPENDIX A

Table A1: Observed T_0s of *Kepler*-279b from Holczer et al. (2016).

Epoch	T_0 [BJD]	σ_{T_0} [days]
0	2454970.73254	0.01319
1	2454982.99776	0.01042
2	2454995.27895	0.01181
3	2455007.57749	0.01319
4	2455019.8316	0.01181
5	2455032.23917	0.01319
6	2455044.5162	0.01597
7	2455056.71753	0.0125
8	2455069.17997	0.00833
9	2455081.48893	0.01111
10	2455093.76455	0.01458
11	2455106.07421	0.01458
12	2455118.41165	0.01458
13	2455130.7227	0.00903
14	2455143.01223	0.01042
16	2455167.62112	0.01181
17	2455179.89467	0.01319
18	2455192.2585	0.01528
19	2455204.62927	0.01181
20	2455216.76393	0.0125
21	2455229.16873	0.02431
22	2455241.48326	0.01389
23	2455253.82695	0.00903
24	2455266.13383	0.00833
25	2455278.43585	0.0125
26	2455290.76913	0.01042
27	2455303.02809	0.00972
28	2455315.37317	0.01042
29	2455327.57242	0.01319
30	2455339.95291	0.01319
31	2455352.26393	0.01458
32	2455364.57846	0.01111
34	2455389.21306	0.00972
35	2455401.54355	0.00972

Epoch	T_0 [BJD]	σ_{T_0} [days]
36	2455413.80946	0.01042
37	2455426.16013	0.01319
38	2455438.49615	0.01389
39	2455450.75439	0.01111
41	2455475.40635	0.00972
42	2455487.73271	0.0125
43	2455499.97707	0.01458
44	2455512.31523	0.00972
45	2455524.61445	0.01181
46	2455536.94011	0.00903
47	2455549.22335	0.01181
49	2455573.84754	0.01042
50	2455586.19334	0.01389
51	2455598.45297	0.00764
52	2455610.7835	0.0125
53	2455623.10355	0.0125
55	2455647.70134	0.01181
56	2455660.0325	0.0125
57	2455672.33456	0.01181
58	2455684.66988	0.01458
59	2455696.94971	0.0125
60	2455709.25726	0.01111
61	2455721.58293	0.0125
62	2455733.8752	0.01181
63	2455746.20086	0.01389
64	2455758.48966	0.01667
66	2455783.13954	0.01111
67	2455795.38673	0.02014
68	2455807.77344	0.01528
69	2455819.94564	0.02292
70	2455832.38791	0.00972
71	2455844.68996	0.01458
72	2455856.90723	0.01806
73	2455869.27867	0.01042
74	2455881.59183	0.0125
75	2455893.95563	0.01458
76	2455906.1806	0.02361
77	2455918.60065	0.01389
78	2455930.7659	0.01597
79	2455943.15753	0.01181
81	2455967.77402	0.0125

Epoch	T_0 [BJD]	σ_{T_0} [days]
82	2455980.06565	0.01389
83	2455992.32604	0.01319
84	2456004.687	0.01111
85	2456017.03975	0.01181
86	2456029.34805	0.0125
87	2456041.69038	0.01597
88	2456053.96037	0.01042
89	2456066.1284	0.02083
91	2456090.90113	0.01944
92	2456103.19138	0.01458
93	2456115.50732	0.01528
95	2456140.11825	0.01042
96	2456152.41475	0.01667
97	2456164.74597	0.01181
98	2456177.03622	0.02778
99	2456189.3562	0.01042
100	2456201.57979	0.01389
101	2456213.89712	0.01389
102	2456226.21445	0.0125
103	2456238.5761	0.00972
105	2456263.19271	0.01389
106	2456275.51478	0.01736
107	2456287.82864	0.00764
108	2456300.14944	0.01736
110	2456324.74509	0.0125
111	2456337.05479	0.01042
112	2456349.39364	0.01319
113	2456361.69639	0.00833
114	2456374.09971	0.01597
115	2456386.29065	0.01042
116	2456398.59549	0.01042
117	2456410.90726	0.01042
118	2456423.18767	0.01528

Table A2: Observed T_0s of *Kepler*-279c from Holczer et al. (2016).

Epoch	T_0 [BJD]	σ_{T_0} [days]
0	2454984.07635	0.00507
1	2455019.80741	0.00382
2	2455055.51473	0.00681
4	2455126.99922	0.00521
5	2455162.78631	0.00694
6	2455198.49566	0.00833
7	2455234.26935	0.00632
8	2455270.0048	0.00674
9	2455305.77432	0.00833
10	2455341.49141	0.00507
11	2455377.24965	0.00438
12	2455413.00622	0.00465
13	2455448.72692	0.01111
14	2455484.46776	0.00486
15	2455520.19207	0.00694
17	2455591.66083	0.00583
18	2455627.41348	0.00514
19	2455663.13772	0.00764
20	2455698.85113	0.00493
21	2455734.58655	0.00528
22	2455770.37552	0.00174
23	2455806.03629	0.00347
24	2455841.76665	0.00597
25	2455877.49533	0.00674
26	2455913.21346	0.00833
27	2455948.94924	0.00417
28	2455984.67723	0.00764
29	2456020.41577	0.00764
30	2456056.14377	0.00903
31	2456091.82676	0.01319
33	2456163.30976	0.00632
34	2456199.05754	0.00764
35	2456234.78832	0.00528
36	2456270.5329	0.00493
37	2456306.29387	0.00833
38	2456342.20521	0.00764
39	2456377.80695	0.00764
40	2456413.50919	0.00535

Table A3: Observed T_0s of *Kepler*-279d from Holczer et al. (2016).

Epoch	T_0 [BJD]	σ_{T_0} [days]
0	2454981.92871	0.00764
1	2455036.37671	0.00694
2	2455090.73699	0.00507
3	2455145.09632	0.00972
4	2455199.50266	0.00972
5	2455253.82357	0.00833
7	2455362.6084	0.00535
8	2455416.98007	0.00694
9	2455471.41212	0.00694
10	2455525.7723	0.00604
11	2455580.24289	0.00403
12	2455634.64217	0.01597
13	2455689.1138	0.01806
14	2455743.51453	0.0066
15	2455797.97367	0.00611
16	2455852.4328	0.00764
17	2455906.85103	0.00694
18	2455961.29551	0.01458
20	2456070.18977	0.00549
22	2456179.00796	0.00625
23	2456233.4203	0.00646
24	2456287.82539	0.00361
25	2456342.17314	0.01042
26	2456396.57416	0.00632

BIBLIOGRAPHY

Agol, E. & Fabrycky, D. C. 2017, in Handbook of Exoplanets, ed. H. J. Deeg & J. A. Belmonte (Springer International Publishing), 1

Agol, E. et al. 2005, MNRAS, 359, 567

Andrae, R. et al. 2018, A&A, 616, A8

Becker, J. C. et al. 2015, ApJ, 812, L18

Borkovits, T. et al. 2002, A&A, 392, 895

Borsato, L. et al. 2014, A&A, 571, A38

Cash, J. R. & Karp, A. H. 1990, ACM Trans. Math. Softw., 16, 201

Charbonneau, P. 1995, ApJS, 101, 309

Chatterjee, S. & Tan, J. C. 2014, ApJ, 780, 53

Chen, J. & Kipping, D. 2017, ApJ, 834, 17

Deck, K. M. & Agol, E. 2015, ApJ, 802, 116

Deck, K. M. & Agol, E. 2016, ApJ, 821, 96

Duncan, M. J., Levison, H. F., & Lee, M. H. 1998, AJ, 116, 2067

Eberhart, R. C. 2007, Computational Intelligence: Concepts to Implementations (San Francisco, CA, USA: Morgan Kaufmann Publishers Inc.)

Evans, D. W. et al. 2018, A&A, 616, A4

Fabrycky, D. C. 2010, in Exoplanets, ed. S. Seager (The University of Arizona Press), 217

Ford, E. B. et al. 2012, ApJ, 756, 185

Foreman-Mackey, D. et al. 2013, PASP, 125, 306

Gaia Collaboration et al. 2018, A&A, 616, A1

Gillon, M. et al. 2017, Nature, 542, 456

Goldberg, D. E. 1989, Genetic Algorithms in Search, Optimization and Machine Learning, 1st edn. (Boston, MA, USA: Addison-Wesley Longman Publishing Co., Inc.)

Goodman, J. & Weare, J. 2010, Communications in Applied Mathematics and Computational Science, 5, 65

Gray, D. F. 1967, ApJ, 149, 317

Hadden, S. & Lithwick, Y. 2014, ApJ, 787, 80

Hadden, S. & Lithwick, Y. 2017, AJ, 154, 5

Handley, W. J., Hobson, M. P., & Lasenby, A. N. 2015, MNRAS, 453, 4384

Hartman, J. D. & Bakos, G. Á. 2016, Astronomy and Computing, 17, 1

Holczer, T. et al. 2016, ApJS, 225, 9

Holman, M. J. & Murray, N. W. 2005, Science, 307, 1288

Holman, M. J. et al. 2010, Science, 330, 51

Kipping, D. M. 2014, MNRAS, 440, 2164

Kollerstrom, N. 2001, A Neptune Discovery Chronology (University College London)

Kovács, G., Zucker, S., & Mazeh, T. 2002, A&A, 391, 369

Kreidberg, L. 2015, PASP, 127, 1161

Laskar, J. 1993a, Physica D: Nonlinear Phenomena, 67, 257

Laskar, J. 1993b, Celestial Mechanics and Dynamical Astronomy, 56, 191

Laskar, J. 1999, in Hamiltonian Systems with Three or More Degrees of Freedom, ed. C. Simó (Dordrecht: Springer Netherlands), 134

Laskar, J., Froeschlé, C., & Celletti, A. 1992, Physica D: Nonlinear Phenomena, 56, 253

Lissauer, J. J. et al. 2011, Nature, 470, 53

Lithwick, Y., Xie, J., & Wu, Y. 2012, ApJ, 761, 122

Mandel, K. & Agol, E. 2002, ApJ, 580, L171

Marzari, F., Scholl, H., & Tricarico, P. 2006, A&A, 453, 341

Marzari, F., Tricarico, P., & Scholl, H. 2002, ApJ, 579, 905

Masuda, K. 2014, ApJ, 783, 53

Mathur, S. et al. 2017, ApJS, 229, 30

Mayor, M. & Queloz, D. 1995, Nature, 378, 355

Miralda-Escudé, J. 2002, ApJ, 564, 1019

Morton, T. D. et al. 2016, ApJ, 822, 86

Murray, C. D. & Dermott, S. F. 2000, Solar System Dynamics (Cambridge University Press)

Nesvorný, D. & Beaugé, C. 2010, ApJ, 709, L44

Nesvorný, D. & Morbidelli, A. 2008, ApJ, 688, 636

Nesvorný, D. et al. 2012, Science, 336, 1133

Nesvorný, D. et al. 2013, ApJ, 777, 3

Perryman, M. 2014, The Exoplanet Handbook (Cambridge University Press)

Petigura, E. A., Marcy, G. W., & Howard, A. W. 2013, ApJ, 770, 69

Rowe, J. F. et al. 2014, ApJ, 784, 45

Sanders, J. L. & Das, P. 2018, ArXiv e-prints

Schmitt, J. R. et al. 2014, ApJ, 795, 167

Seager, S. & Mallén-Ornelas, G. 2003, ApJ, 585, 1038

Smith, J. C. et al. 2012, PASP, 124, 1000

Steffen, J. H. 2016, MNRAS, 457, 4384

Sterken, C. 2005, in The Light-Time Effect in Astrophysics: Causes and cures of the O-C diagram, ed. C. Sterken, Vol. 335, 3

Tada, T. 2007, JSHWR, 20, 450

Tamuz, O., Mazeh, T., & North, P. 2006, MNRAS, 367, 1521

Ulrich, R. K. 1986, ApJ, 306, L37

Van Eylen, V. et al. 2018, ArXiv e-prints

Weiss, L. M. & Marcy, G. W. 2014, ApJ, 783, L6

Wolfgang, A., Rogers, L. A., & Ford, E. B. 2016, ApJ, 825, 19

Xie, J. W. 2014, ApJS, 210, 25

RINGRAZIAMENTI

Vorrei, innanzitutto, esprimere la mia riconoscenza al mio relatore, Giampaolo Piotto, a Valerio, e a tutte le persone dell'ESPG, per avermi permesso di approfondire gli argomenti che mi appassionano, per avermi accolto nel team e guidato in questo lavoro di tesi. Un ringraziamento particolare a Luca, per la sua infinita pazienza, le innumerevoli spiegazioni, le ore spese a correggere le mie bozze e, soprattutto, per non avermi mai scacciata dall'ufficio ogni volta che mi sono affacciata alla porta.

Un ringraziamento va poi alla mia squadra di astronome: insieme dal primo anno, senza di voi non avrei mai affrontato con la stessa determinazione (e fretta) quella lunghissima serie di esami. Alla mia coppia preferita, grazie per avermi accolto come reggi-candela senza avermi mai fatto sentire di troppo: o dovrei forse ringraziare l'Amore?
Devo *ben* ringraziare anche tutti i miei amici, di su e di giù, per esserci sempre stati quando c'era bisogno, per i disegni artistici del Re Leone, per le feste, le riunioni, le discussioni, i the caldi e i verbali. Un particolare abbraccio alla mia Bionda, che dal letto accanto ha seguito alti e bassi di questo cammino, sempre pronta ad offrirmi le consolazioni di Biasetto.

Grazie a mio fratello, per essermi corso incontro ogni volta che mi affacciavo alla porta di casa. A papà, per essere la persona più integra che io conosca, una vera forza della natura. E alla mamma, per essere così paziente, altruista e affettuosa, approdo sicuro in ogni tempesta: per tutto quel che mi avete dato, questo traguardo è mio tanto quanto vostro.

E, concludendo, grazie infinite a te, Francesco (anche se credi in una scienza che chissà se esiste), per essere il mio sostegno e la mia forza, sempre.